A multi-isotope and modelling approach for constraining hydro-connectivity in the East African Rift System, southern Ethiopia

*[1,2]Markowska, M., [3]Martin, A.N., [2]Vonhof, H. B., [2,4,5]Guinoiseau, D., [1,6]Fischer, M.L, [7,8]Zinaye, B., [2]Galer, S.J.G., [8]Asrat A., [1,6]Junginger, A.

[1]University of Tübingen, Department of Geosciences, Tübingen, Germany.

[2]Max Planck Institute for Chemistry, Climate Geochemistry Department, Mainz, Germany.

[3]Leibniz University Hannover, Institute of Mineralogy, Hannover 30171, Germany.

[4]Université de Paris, Institut de physique du globe de Paris, CNRS, F-75005 Paris, France.

[5]Aix Marseille Univ, CNRS, IRD, INRAE, Coll France, CEREGE, Aix-en-Provence, France.

[6]Senckenberg Centre for Human Evolution and Paleoenvironment (S-HEP), Tübingen, Germany.

[7] University of Cologne, Department of Geosciences, Cologne, Germany.

[8]Addis Ababa University, School of Earth Sciences, Addis Ababa, Ethiopia.

*Corresponding author: monika.markowska@mpic.de

Keywords: Lake Chew Bahir: isotope-enabled hydro-balance model: $^{87}Sr/^{86}Sr$: $\delta^{18}O$: African Humid Period

Abstract

During the last African Humid Period (AHP; 15-5 ka), many lakes in the East African Rift System (EARS) experienced pronounced lake level variations that dramatically transformed the hydrological landscape. Currently dry, saline or marshy-wetland terminal lakes became vast waterbodies, interconnected via overflow sills resulting in the formation of a several thousand-kilometre-long chain of lakes in the EARS. A quantitative, processed-based understanding of these hydrological systems can advance our interpretation of past hydroclimate variability. Here, we provide a critical modern hydrological dataset for the data sparse Lake Chew Bahir basin, southern Ethiopia. Driven by modern data, an isotope-enabled hydro-balance model was developed to assess how increases in rainfall modulate $\delta^{18}O$ and $^{87}Sr/^{86}Sr$ variability. Considering a terminal lake scenario in Lake Chew Bahir under humid conditions resulted in higher lake $\delta^{18}O$ (~+12‰) due to increased evaporation and longer water residence times, whereby $^{87}Sr/^{86}Sr$ decreased from 0.7064 to 0.7062 due to an increased riverine Sr flux characterised by lower, unradiogenic $^{87}Sr/^{86}Sr$ ratios. Assuming a flow-through lake scenario with interconnectivity between lakes Abaya, Chamo, Chew Bahir and Turkana resulted in higher lake $\delta^{18}O$ (~+8‰) relative to present, but lower than in terminal lake conditions, coupled with lower $^{87}Sr/^{86}Sr$ ratios (<0.7061). Modelled $\delta^{18}O$ were similar to the $\delta^{18}O$ range of endogenic carbonates from sedimentary cores from Lake Chew Bahir at the onset of the AHP, supporting the validity of our model and suggesting that evaporation and the lake water residence time strongly influence lake water $\delta^{18}O$. However, the reported $^{87}Sr/^{86}Sr$ of fossil carbonates from Lake Chew Bahir during the AHP (0.7065-0.7060) could not be reproduced by our modelled scenarios without adjusting the surface water-to groundwater ratio, highlighting the potential role of groundwater as a water source in semi-arid regions. These results demonstrate the insights that can be gained from applying a process-based approach using O and Sr isotope hydro-balance modelling to aid

interpretation of past hydro-balance and lake interconnectivity from lacustrine sedimentary records.

1 Introduction

The East African Rift System (EARS) contains 80+ lake systems (Schagerl and Renaut, 2016), many of which filled and overflowed, becoming interconnected during the most recent late Pleistocene to mid-Holocene pluvial episode, the African Humid Period (AHP) (Beck et al., 2019; Forman et al., 2014; Junginger and Trauth, 2013; Talbot et al., 2000). Since the AHP, some of these lakes, such as Lake Chew Bahir (LCB) in southern Ethiopia, receded into small endorheic marshes and wetlands (Fischer et al., 2020; Foerster et al., 2012). A particular feature of the EARS lakes is their sensitivity to climatic variability due to higher precipitation rates on the high-elevation rift margins, coupled with high evaporation rates in the lower-elevation rift floors and have subsequently been termed 'amplifier lakes'(Street-Perrott and Harrison, 1985; Trauth et al., 2010).

Recurring extreme drought and flood conditions are common in the EARS, even on annual timescales. Recently, above average rainfall triggered a humanitarian crisis resulting in the displacement of people, food insecurity, death and property destruction, impacting over 27 million people in eastern Africa since March 2020 alone (OCHA, 2020). Extreme hydroclimate variability at LCB in southern Ethiopia however is not a new phenomenon. Rapid shifts from wet to dry conditions were reported in carbonate lake core records during 116-66 ka BP, transitioning to a more stable, drier period between 58 and 32 ka BP (Viehberg et al., 2018), which is also indicated by trace element variations in lacustrine sediments during 45-35 ka BP (Foerster et al., 2012). Elemental abundances in the sedimentary cores from 23 to 5 ka BP, in contrast, broadly followed a similar trend to precession-forced insolation increases, interpreted as wet conditions during the AHP (15-5 ka BP), punctuated by large changes in K abundances interpreted as rapid oscillations from wet to dry conditions (Foerster et al., 2012). However, it is difficult to translate proxy records to

quantify changes in lake level, or identify the dominant sources of hydrological reorganisation (provenance).

Strontium (Sr) isotopic ratios ($^{87}Sr/^{86}Sr$) of lacustrine carbonates and bioapatite preserved in paleo-shoreline deposits or recovered from sedimentary cores in the EARS may be used to reconstruct provenance of hydrological inputs and assess past changes in regional water balance (Baddouh et al., 2016; Doebbert et al., 2014; Hart et al., 2004; Joordens et al., 2011; Talbot et al., 2000; van der Lubbe et al., 2017). Appreciable amounts of calcium carbonate were precipitated in Lake Chew Bahir over the AHP in the form of stromatolites, molluscan shells, and ostracods, as well as bioapatite such as fish bones and teeth. Strontium is present in these carbonates in trace amounts (10-1000s ppm). Since any Sr isotope fractionation (natural or analytical) is corrected for during radiogenic Sr isotope analysis, physical or chemical isotope fractionation processes in the lake do not influence the $^{87}Sr/^{86}Sr$ ratio measured in lacustrine fossil carbonates. Consequently, the Sr isotope ratio of lake biota directly record the Sr isotope composition of lake waters (Hart et al., 2004). This is particularly useful in EARS catchments which have widely varying $^{87}Sr/^{86}Sr$ end-members; for example, Precambrian metamorphic-granitic and gneissic rocks with more radiogenic $^{87}Sr/^{86}Sr$ and Cenozoic flood basalts with less radiogenic $^{87}Sr/^{86}Sr$ (Table 1).

Quaternary climate reconstructions probing $^{87}Sr/^{86}Sr$ in lacustrine carbonate fossils from Lake Turkana (adjacent to LCB) found that lake water $^{87}Sr/^{86}Sr$ was controlled by inflow variability from the Omo River to the north and the Turkwel and Kerio Rivers to the south during the AHP (van der Lubbe et al., 2017), whereas on longer timescales (~2.0-1.7 Ma) were suggested to be governed exclusively by changes in surface inflows of the Omo River (Joordens et al., 2011). Both studies emphasised that $^{87}Sr/^{86}Sr$ in Lake Turkana is insensitive to interannual fluctuations and only responds to long-term orbitally induced forcing. As $^{87}Sr/^{86}Sr$ changes with hydrological inflows, it has also been used to infer paleo lake levels.

For example, variations of paleo $^{87}Sr/^{86}Sr$ in the Bonneville paleolake system, U.S., can be directly attributed to lake levels and changes in the contribution of the Bear River to the dissolved Sr flux (Hart et al., 2004).

Table 1. Mean Sr concentration and $^{87}Sr/^{86}Sr$ of rocks sampled in southern Ethiopia and northern Kenya. Precambrian metamorphic average $^{87}Sr/^{86}Sr$ values here are also in agreement with the measured bioavailable $^{87}Sr/^{86}Sr$ from catchments dominated by Precambrian-aged lithology (0.72796) (Janzen et al., 2020).

Southern Ethiopia

Period/Eon	**$^{87}Sr/^{86}Sr$**	**Sr**	**n**	**Reference**
Precambrian	0.7271±0.0286	323±275	19	Kebede et al., 2003; Kebede et al., 1999; Asrat and Barbey, 2003; Teklay et al., 1998
Neogene/Paleogene	0.7038±0.0004	565±268	43	Shinjo et al., 2011; Stewart and Rogers, 1996; George and Rogers, 2002
Quaternary	0.7028±0.0007	343±378	12	Meshesha et al., 2011; Stewart and Rogers, 1996

Northern Kenya

Neogene/Paleogene	0.7034±0.0005	547±251	10	Furman et al., 2006
Quaternary	0.7043±0.0012	352±301	17	Furman et al., 2006; Clement et al., 2003

Although $^{87}Sr/^{86}Sr$ and $\delta^{18}O$ records from EARS lakes have been successfully used to interpret past changes in climate, there are few modern data available to permit more robust interpretations. For example, 1) whether the riverine $^{87}Sr/^{86}Sr$ reflects that of the average lithology of the catchment area, i.e., congruent weathering conditions, 2) whether the lake $^{87}Sr/^{86}Sr$ and $\delta^{18}O$ are controlled by temporal changes in surface hydrological inflows, 3) the degree and impact of groundwater/surface water interactions, and 4) lake water residence times. Constraining these processes is critical for accurately interpreting $^{87}Sr/^{86}Sr$ and $\delta^{18}O$ records from lacustrine carbonate microfossils and may have significant implications for our understanding of hydrological changes in the EARS.

In this study, we aim to better constrain the controls on lake-water $^{87}Sr/^{86}Sr$ and $\delta^{18}O$ at LCB, southern Ethiopia. LCB is located some 100 km upstream of Lake Turkana, the world's

largest permanent desert lake (Johnson and Malala, 2009). LCB is just a shallow wetland area today, has a much smaller maximum extent than Lake Turkana, and a simpler hydrological system with unidirectional overflow in a north-south direction from hydrological connectivity with upper catchments (Lake Chamo and Lake Abaya) during major humid periods. However, it is analogous to Lake Turkana as it has a similar range of lithological endmembers, and was a large expansive lake during the AHP (Bloszies et al., 2015). Here we specifically aim to determine whether the Sr isotopic composition of catchment waters reflects the $^{87}Sr/^{86}Sr$ of local lithologies and asses the dominant inflows/outflows in terms of hydrological and Sr budgets. Following this, we combine isotopic-mass balance modelling of both Sr and oxygen isotopes, typically expressed as $^{87}Sr/^{86}Sr$ and $\delta^{18}O$ ($^{18}O/^{16}O$), respectively, as the two isotope systems together provide independent constraints on the driving mechanisms of hydrological change in lacustrine systems. Unlike Sr, $\delta^{18}O$ is controlled by the combination of source water inflows (e.g., rainfall, groundwater and surface water) and catchment-integrated evaporation (Cohen et al., 1997; Dettman et al., 2005; Leng and Marshall, 2004; Vonhof et al., 2013), and lake $\delta^{18}O$ records are often interpreted as a proxy for water balance (Chamberlain et al., 2013; Doebbert et al., 2014; Leng et al., 1999). We develop an isotope-enabled hydro-balance model to mechanistically understand O and Sr isotopic variations in LCB and resulting lacustrine carbonates. We extend this to Late Quaternary hydroclimate variability to model the onset of the AHP. This allows us to identify whether catchment hydrological reorganisation explains the change in observed range of Sr isotopes ($^{87}Sr/^{86}Sr$ = 0.7065-0.7060 (van der Lubbe et al., 2017; Junginger et al., unpublished data)) and oxygen isotopes (0.5 to 11 ‰ VPDB) (Viehberg et al., 2018) at LCB during the AHP.

2 Regional setting

2.1 Geology

The LCB catchment is located within the southern MER just northeast of the Turkana Depression, between the Ethiopian and the East African Plateaus (Figure 1d). The metamorphic Precambrian basement rock is dominated by gneisses and granitic intrusions of the Mozambique Belt and the meta-volcano-sedimentary complexes of the Arabian-Nubian Shield (Davidson et al., 1983; Teklay et al., 1998; Asrat et al., 2001; Asrat and Barbey, 2003). Flood basalt volcanism and subordinate trachytic and rhyolitic rocks formed the Ethiopian highlands during the Oligocene while Mid-Miocene to present volcano-tectonic processes involving bi-modal (basaltic and rhyolitic) volcanism characterize the MER (Bonini et al., 2005). The deeper basins of the MER are also covered by Quaternary sediments. The surface lithology of the LCB, Lake Chamo, Lake Abaya and Lake Turkana catchments are quantified in Table 2 and the average $^{87}Sr/^{86}Sr$ of each lithology are summarised in Table 1. The dominant lithology of LCB is Precambrian (40%) and Quaternary sediments (40%), Neogene/Paleogene (17%) and Quaternary volcanics (2%), with the remaining 1% representing the surface covered by the LCB. The greatest proportion of exposed Precambrian basement rocks within LCB sub-catchments are found in the Segen and western dry valley catchments. Neogene/Paleogene volcanics dominate the dry eastern valley (55%) as well as the Abaya and Chamo catchments with 43% and 49% cover, respectively. The Lake Chamo and Lake Abaya catchments have minor contributions from Precambrian metamorphic units in the southeast (6% and 3%, respectively). In comparison, the Lake Turkana catchment is comprised of predominately Paleogene/Neogene volcanic units (52%) with less Precambrian surface cover (20%), which is mainly localised to the Turkwel sub-catchment (68%).

Table 2. Catchment lithology of the LCB, Lake Chamo, Lake Abaya, and Lake Turkana catchments. Catchment shapefiles were used to extract the percentage of rock types in a given catchment using the SEAMIC GSE EN Geology 1:2 million scale Geology Map of Ethiopia and for the northern Kenyan catchments the 1:10M-scale geological map of Africa (Thieblemont, 2016). The catchment lithology for the 'within catchment' samples was calculated from the surface cover for the area upstream of the riverine sample points measured (excluding CB18W08 as it is not connected to a major tributary). The geological fractional mixing model shows the estimated lake and river water $^{87}Sr/^{86}Sr$ and also incorporates the *k* flux (individual *k* fluxes for each catchment and given lithology). Lake areas were assumed to be Quaternary sediments. The lithological end-members Sr concentration and $^{87}Sr/^{86}Sr$ values used can be found in Table 1.

Major catchment	**Chew Bahir**											**Chamo**	**Abaya**	**Turkana**			
Sub-catchment	*Weyto*			*Segen*					*Eastern dry valley*	*Western dry valley*				*Keiro*	*Turkwel*	*Omo*	
within-catchment		*CB18W4*	*CB18W11*		*CB18W1*	*CB18W12*	*CB18W3*	*CB18W16*									
Precambrian Gneissic-granitic	39%	40%	40%	53%	51%	53%	100%	38%	7%	64%	40%	6%	3%	21%	68%	13%	20%
Paleogene/Neogene volcanics	17%	18%	18%	27%	27%	27%	0%	26%	55%	0%	17%	49%	43%	68%	4%	71%	52%
Paleogene/Neogene sedimentary	0%	0%	0%	0%	0%	0%	0%	0%	0%	0%	0%	0%	0%	0%	0%	1%	1%
Quaternary volcanics	0%	0%	0%	6%	7%	15%	0%	17%	0%	0%	2%	0%	32%	0%	0%	0%	1%
Quaternary sediments	44%	42%	42%	15%	15%	6%	0%	19%	39%	36%	40%	27%	15%	12%	28%	16%	21%
Lake	0%	0%	0%	0%	0%	0%	0%	0%	0%	0%	1%	18%	7%	0%	0%	0%	5%
Geological mixing model																	
Measured $^{87}Sr/^{86}Sr$	0.7061	0.7062	0.7064	0.7056	0.7055	0.7055	0.7045	0.7070	n/a	n/a	0.7064	0.7048	0.7062	[a]0.7054	[a]0.7083	[a]0.7051	[a]0.7051
Estimated $^{87}Sr/^{86}Sr$	0.7065	0.7064	0.7064	0.7062	0.7061	0.7061	0.7271	0.7055	n/a	n/a	0.7065	0.7040	0.7039	0.7039	0.7140	0.7041	0.7040
Geological mixing model +weathering flux (k)																	
Estimated $^{87}Sr/^{86}Sr$	0.7061	0.7062	0.7061	0.7056	0.7055	0.7055	0.7271	0.7070	n/a	n/a	0.7064	0.7048	0.7062	0.7054	0.7083	0.7051	0.7051

Precambrian *k*	1	1	1	1	1	1	1	1	n/a	n/a	1	1	1	1	1	1	1
Paleogene/Neogene *k*	1.2	1.0	1.1	1.2	1.3	1.3	0.0	0.5	n/a	n/a	1.0	0.2	0.0	0.2	3.9	0.2	0.3
Quaternary sediments *k*	1.1	1.0	1.1	1.2	1.3	1.3	0.0	0.5	n/a	n/a	1.0	0.4	0.8	0.7	4.3	0.2	0.3
Quaternary volcanics *k*	1.1	1.0	1.1	1.2	1.3	1.3	0.0	0.4	n/a	n/a	1.0	0.2	0.0	0.7	3.9	0.2	0.3

[a]Data from van der Lubbe et al. (2017).

2.2 Climate

The Koppen climate classification for the southernmost area of the LCB catchment is hot semi-arid (Precipitation<Evaporation). The central-northern LCB catchment, Lake Chamo and Lake Abaya fall into the tropical savannah with higher rainfall, despite severe dry seasons with frequent droughts. The LCB catchment has two rainy seasons, the longer season from March to May, and the shorter season from October to November, with ~500 mm a^{-1} (Figure 1b). The highlands northwest of LCB, including the Lake Abaya and Lake Chamo catchments, experience significantly higher (~>1000 mm a^{-1}; Figure 1b) and unimodal rainfall spanning March to November (Segele and Lamb, 2005; Williams and Funk, 2011).

2.3 Hydrology

Lake Chew Bahir (498 m a.s.l.) is an ephemeral wetland at its northerly extent (Figure 1c), which intermittently fills in a southerly direction in the wet seasons (Figure 1d) with a maximum lake surface area of 2486 km^2 (Fischer et al., 2020). LCB's volume fluctuates considerably; from complete desiccation at least once in the 19th century to a 2000 km^2 lake in 1960 CE (Golubtsov and Habteselassie, 2010), and a reported 8 m depth in the late 19th century (Grove et al., 1975). It is perennially fed by the Weyto and Segen rivers (Figure 2), which drain the north-western and north-eastern sides of the catchment, respectively. The Weyto River is the source of the majority of surface inflows with an average flow rate of 72 m^3/s (2.27 km^3/a) approximately thrice that of the Segen (Supplementary Table 1) (JICA, 2012). The tectonic basin is bound by the Teltele-Konso Plateau and the Hammar Range in the east and west, respectively. The LCB basin overflows in a southerly direction to Lake Turkana in northern Kenya, when the overflow sill is surpassed (543 m a.s.l.), which does not occur under the modern climate regime. Overflow sill elevations, lake water surface areas and locations are given in Table 3. To the northeast lies Lake Chamo and Lake Abaya (Figure 1b). Lake Abaya (1176 m a.s.l.) occasionally connects to Lake Chamo via an overflow sill at

1194 m a.s.l. during high rainfall periods, although this is infrequent under the modern climatic regime where lake levels only fluctuate by 0-1 m (Belete et al., 2015). The smaller Lake Chamo (1109 m a.s.l.) connects to LCB catchment via an overflow sill at 1123 m a.s.l. via the Segen River when precipitation exceeds the long-term average (Belete et al., 2015).

Table 3. General characteristics of Lake Chew Bahir (LCB) Lake Chamo (LC) and Lake Abaya (LA). Surface area data from Fischer et al.(Fischer et al., 2020).

	LCB	LC	LA
Latitude (°N)	4.857 - 4.766	5.966 - 5.709	6.589 - 5.774
Longitude(°E)	36.911 - 36.888	37.552 - 37.627	37.616 - 38.051
Elevation (m a.s.l.)	498	1,109	1,176
Modern lake surface area (km^2)	~43	310	1,081
Maximum lake surface area (km^2)	2,486	394	1,557
Modern maximum water depth (m)	1-2	13	13
Overflow elevation (m a.s.l.)	543	1,123	1,194

Groundwater flow in the LCB basin generally follows the surface topography along a north-south gradient in the direction of Lake Turkana (JICA, 2012). Recharge typically occurs on the elevated rift margins which receive more rainfall (Bretzler et al., 2011). There are three main aquifer types in the basin which relate to the three geological units; granitic-gneissic basement rocks; volcanic rocks and Quaternary sediments and alluvium. Crystalline basement rock aquifers, such as those in the Hammar Range, receive localised recharge associated with fracture and intergranular permeability and have low storage potential. The second type are extensive volcanic aquifers with fracture permeability which experience localised recharge with low storage potential and hydraulic conductivity. The third type is low elevation rift floor unconsolidated sediments and alluvium and higher elevation marginal/alluvial grabens (Kebede et a., 2010).

Previous hydrogeological investigation has been mainly focused around the central MER, with very limited data in the southern MER from commercial reports (e.g. JICA, 2012, Halcrow et al., 2008). Due to the low porosity and storage potential of LCB basin aquifers, most of the groundwater potential is localised in shallow wadi bed sediments overlaying basement rocks. Recharge typically occurs through wadi sediments which is enhanced during flooding events, commonly allowing localised recharge 'pulses' to occur. Groundwater discharge typically occurs in the direction of the rift flanks towards the rift floor via stream baseflow (Kebede et al., 2010b) and spring discharge is <1-5 l/s (JICA, 2012). There is a general increase in the overall salt content of groundwaters and concomitant change in chemistry from Ca-Mg HCO_3 in the highlands to Na-HCO_3-SO_4Cl type in the rift floor due to solute remobilization from lacustrine sediment thin evaporite lenses (Tessema in Kenbede 2010). Groundwater flow between Ethiopia and Kenya is considered to be negligible as lacustrine sediments contain impermeable clay layers (JICA, 2012; Foerster et al., 2012).

3 Methods

3.1 Field procedures

In November 2018, 20 water samples were collected during a field campaign in the LCB catchment, and Lake Chamo and Lake Abaya (Figure 2). Due to LCB's remote location and difficulty of access, there are hardly any published data (hydrochemistry, Sr and O isotope data) for the LCB catchment to date, to the best of the authors' knowledge. Here, we provide the first small-scale catchment wide study of LCB. We also note that areas such as the eastern dry catchments and large parts of the south-eastern margins of the LCB basin were inaccessible due to security concerns . These areas still warrant further investigation.

Seven groundwater samples were collected from frequently pumped (all wells were being actively used prior to sampling) driven point wells (India Mark II wells that are

common in rural communities in eastern Africa) of <50 m depth. Prior to sampling, the wells were purged until the in situ measurements stabilised, including pH, electrical conductivity (EC), total dissolved solids (TDS), temperature and oxidation reduction potential (ORP) using a HI98194 (Hanna Instruments) multi-meter instrument. Five lake samples were collected from LCB (n = 2), Lake Chamo (n = 2) and Lake Abaya (n = 1) as well as seven samples from the Weyto and Segen Rivers and their tributaries and one cold spring (Figure 2). Total alkalinity concentrations were measured using the endpoint titration method and a Hach digital titrator within 24 hours of sampling. Samples for anions and stable water isotopes ($\delta^{18}O$ and $\delta^{2}H$) were immediately filtered through 0.45 μm nylon filters and collected in 60 ml High Density Poly-Ethylene (HDPE) bottles and 5.9 ml exetainer® glass vials (Labco), respectively, with no further treatment. Cation, $^{87}Sr/^{86}Sr$ and trace element samples were collected in 60 ml acid-cleaned HDPE bottles, and immediately acidified with ~1 ml of Suprapur® (Merck) 65% HNO_3.

3.2 Chemical analysis

Cation and anion concentrations were analysed using ion chromatography compact IC Flex and Compact IC Plus from Metrohm at the University of Tübingen, Germany. The limits of detection were as follows Na (0.1 ppm), K, Ca, Mg, Cl, PO_4 (0.05 ppm), F (0.005 ppm), SO_4 (0.5 ppm). $\delta^{18}O$, $\delta^{2}H$ and $^{87}Sr/^{86}Sr$ were analysed at the Max Planck Institute for Chemistry in Mainz , Germany. $\delta^{18}O$ and $\delta^{2}H$ were measured using a Picarro cavity ring down laser spectrometer and are reported as a per mil (‰) deviation from the international standard VSMOW. The overall precision on analyses were ±0.1‰ $\delta^{18}O$ and ±1.1‰ $\delta^{2}H$ (2σ, n =15). For $^{87}Sr/^{86}Sr$ analyses, Sr was separated from samples using DGA resin (Eichrom), using a prep*FAST*-MC™ system (Elemental Scientific) based on the method from Romaniello et al. (2015). Approximately 100 ng of purified Sr was then loaded onto tungsten filaments with Ta-fluoride activator and $^{87}Sr/^{86}Sr$ was measured using a ThermoFisher

Triton™ Thermal Ionisation Mass Spectrometer. Replicate measurements of NIST SRM-987 run with these samples yielded an average $^{87}Sr/^{86}Sr$ value of 0.71026 ± 0.00001 (2σ, n = 8).The Sr concentrations of the total procedural blanks were below the limit of detection (<0.3 ppb).

3.3 Coupled $\delta^{18}O$ and $^{87}Sr/^{86}Sr$ mass balance modelling

3.3.1 $\delta^{18}O$ model

A $\delta^{18}O$-enabled mass balance lake model (Gibson et al., 2016) was used to quantify modern lake balance sensitivity and paleo-changes in $\delta^{18}O$ lake composition based on well-established previous models (Craig and Gordon, 1965; Gat, 1996; Gibson and Edwards, 2002; Gonfiantini, 1986; Horita et al., 2008; Jones et al., 2016). The lake water volume (km^3 a^{-1}) is given as:

$$\frac{dV}{dt} = P + Q_i - E - Q_o \quad (1)$$

where V is the volume (km^3) at time t (a^{-1}), P is precipitation volume (km^3 a^{-1}) on the maximum lake surface area per unit time (2,486 km^2 (Fischer et al., 2020)), E is evaporation (km^3 a^{-1}) from the lake surface per unit time, Q_i and Q_o are the surface inflows and outflows (km^3 a^{-1}), respectively (Supplementary Table 1).

To parameterise flow, the average annual discharge estimated from gauge flow data from the Weyto River (27 years of data, station ID: 083002 (JICA, 2012)) and Segen River (3 years of data, station ID: 083001(JICA, 2012)) was used, which yielded annual inflows of 2.27 and 0.71 km^3 a^{-1}, respectively. Groundwater discharge (G_i) is difficult to estimate due to highly variable flow rates (Mechal et al., 2017) and fluctuating water tables which vary significantly over short distances (Ayenew et al., 2008; Furi et al., 2012; Kebede et al., 2007; Tenalem et al., 2009). Here, a mass balance approach was used to determine groundwater input based on

the flow parameters and measured $^{87}Sr/^{86}Sr$ ratios and concentrations (Supplementary Table 1) to give a groundwater inflow (G_i) of ~0.25 $km^3\ a^{-1}$.

The isotopic composition of the lake mass (‰) was calculated by assuming that the lake is well-mixed and has a constant water density, which is given as:

$$\frac{d}{dt}(V\delta_L) = P\delta_P + Q_i\delta_i - E\delta_E - Q_o\delta_L \quad (2)$$

δ_P, δ_i, δ_E, and δ_L are the isotopic composition of precipitation, inflows, evaporation and LCB, respectively. The equation was rearranged and integrated to solve for δL following the integration steps in Equations 9 to 13 from Jones et al. (2016), using an annual time step where flux terms, such as E, vary at each time step and as such take different values to account for the changing lake volume. The term $Q_i\delta_i$ is defined as:

$$Q_i\delta_i = R_i\delta_i + G_i\delta_{gi} + L_i\delta_{li} \quad (3)$$

where δ_{gi} with an isotopic composition of G_i, and L_i is the lake overflow from Lake Chamo with isotopic composition of δ_{li}. Lake Chamo overflow into LCB is initiated if P exceeds 2% of modern P, based on previous DEM and overflow lake balance modelling output (Fischer et al., 2020), at a rate of 10% of the volume of the Segen River at each time step, as the natural overflow of LC is via the Segen River. The term R_i represents the riverine input and is given as:

$$R_i = S_i\delta_{si} + W_i\delta_{wi} \quad (4)$$

where S_i is the inflow from the Segen River, with isotopic composition δ_{si} and W_i is the inflow from the Weyto River with a mean isotopic composition of δ_{wi}.

The term $Q_o\delta_L$ is defined as:

$$Q_o\delta = G_o\delta_L + L_o\delta_L \quad (5)$$

where G_o is the groundwater recharge, calculated as the residual of Equation 1 assuming steady state conditions ($Q_i = Q_o$), for an estimated modern LCB volume of 0.15 km^3, yielding an annual outflow to recharge of 2.84 $km^3\ a^{-1}$. L_o is the surface overflow from LCB to Lake Turkana, calculated as the surplus volume greater than 83.17 km^3 – the maximum extent of LCB (Fischer et al., 2020).

The δ_P of P is the calculated mean annual isotopic composition of rainfall calculated for the LCB area using the Online Isotopes in Precipitation Calculator (https://wateriso.utah.edu/waterisotopes/pages/data_access/form.html) (see Section 4.1.1). The O, H and Sr isotopic compositions of the other inflows were determined from the end-members of samples from the 2018 field campaign, which were taken in between the dry and the rainy seasons (Supplementary Table 1). The most downstream samples (closest to LCB) before the confluence point of the two rivers were designated as δ_{si} and δ_{wi}. Average groundwater $\delta^{18}O$ from the 7 sampled sites was used for the groundwater end-member (δ_{gi}). The value for δ_{li} (overflow into LCB) is the average of measured Lake Chamo water.

As δ_E is difficult to measure, it is typically calculated (Skrzypek et al., 2015) using the Craig and Gordon (Craig and Gordon, 1965) evaporation model, given as:

$$\delta_E = \frac{\alpha^+\delta_L - h\delta_A - \varepsilon}{1-h+0.001\varepsilon_k} \quad (‰) \tag{6}$$

where a^+ is the equilibrium isotopic fractionation factor that is dependent on the measured temperature at the evaporating lake surface and is derived from experimental values (Horita and Wesolowski), given as:

$$\alpha^+(^{18}O) = \exp\left(-\frac{7.685}{10^3} + \frac{6.7123}{273.15+T} - \frac{1666.4}{(273.15+T)^2} + \frac{350410}{(273.15+T)^3}\right) \tag{7}$$

where T is the temperature of the lake surface (°C), h is the relative humidity corrected for the saturation vapour pressure (Supplementary Table 1), εk is the kinetic fractionation factor defined as 14.2(1- h) (Gonfiantini, 1986) and δA is the isotopic value of the air vapour over the lake assuming atmospheric moisture is at equilibrium with P given by:

$$\delta_A = (\delta_P - \varepsilon^+)/(1 + 10^{-3} \cdot \varepsilon^+) \quad (‰) \tag{8}$$

where $\varepsilon^+ = 1000(1\text{-}\alpha^+)$ (Gibson et al., 2016). Equation 9 gives an expression for δ_L at time t, on a yearly timestep (dV/dt approximated as equal to the change in volume over 1 year).

$$\delta_L(t) = \delta_s - (\delta_s - \delta_o) \exp\left[-(1 + mx)\left(\frac{It}{V}\right)\right] \quad (‰) \tag{9}$$

δ_s is the steady state isotopic composition of the lake given by Gonfiantini (1986) and Gat (1996) as t approaches ∞, where δ_0 is the initial isotopic composition of the lake at t_0 and δ_I is the total isotopic composition of inflows.

$$\delta_s = (xm\delta^* + \delta_I)/(1 + mx) \quad (‰) \tag{10}$$

Here m and x are dimensionless and defined as:

$$m = \frac{(h - 10^{-3}\left(\varepsilon k + \frac{\varepsilon^+}{\alpha^+}\right))}{(1 - h + 10^{-3} * \varepsilon k)} \quad \text{(dimensionless)} \tag{11}$$

and

$$x = (\delta_s - \delta_I/(m(\delta^* - \delta_s)) \quad \text{(dimensionless)} \tag{12}$$

Finally, we calculated open water E of 1,908 mm a^{-1} from Fischer et al. (2020) using the Penmann-Monteith equation relative to the evaporating surface area of LCB. E was calculated at a rate of 1,908 mm a^{-1} with changing surface area at each yearly time step. Based on modern lake surface area this gave an initial E volume of 0.39 km^3 a^{-1} to initialise the model. For ease of calculation surface area was calculated indirectly from DEM model output from Fischer et al. (2020) using an empirical relationship between volume and surface area calculated specifically for LCB and given in Supplementary Figure 1.

3.3.2 Sr model

To estimate the sensitivity of LCB to temporal changes in Sr fluxes from sub-catchments and overflow from adjacent basins we used a Sr model from Hart et al. (2020) combined with our O isotope model. The simple mass balance model is given by:

$$^{87}Sr/^{86}Sr_{lake} = f_{Sr\ Weyto}(^{87}Sr/^{86}Sr_{Sr\ Weyto}) + f_{Sr\ Segen}(^{87}Sr/^{86}Sr_{Sr\ Segen}) + f_{Sr\ groundwater}(^{87}Sr/^{86}Sr_{Sr\ groundwater}) + f_{Sr\ Lake\ Chamo}(^{87}Sr/^{86}Sr_{Sr\ Lake\ Chamo}) + f_{Sr\ P}(^{87}Sr/^{86}Sr_{Sr\ P}) \quad (13)$$

where f is the fraction of Sr from each major Sr flux (Supplementary Table 1). Average $^{87}Sr/^{86}Sr$ values from the water sampling campaign were used for the riverine, lake and groundwater end-members. Sample CB18W8 was excluded as it was a small tributary of the Weyto River, and we could not confirm its flow routing connectivity to the greater Weyto River in the field. The Sr contribution from rainfall (f_{SrP}) to lake water is typically low and was not considered significant due to the inland location (~1000 km from Indian Ocean) of LCB.

3.3.3 Model parameters

To assess how lake water $\delta^{18}O$ and $^{87}Sr/^{86}Sr$ records respond to regional climate change and hydrological reorganisation, three scenarios were considered with varying degrees of catchment connectivity: 1) Closed terminal LCB, 2) Semi-open terminal LCB (overflow from Lake Chamo activated), and 3) Open flow-through LCB (LCB overflows to Lake Turkana; Table 4). In scenario three, full cascading lake connectivity is assumed whereby Lake Abaya, Lake Chamo, LCB and Lake Turkana are a cascading lake system and consequently Lake Turkana is significantly larger than present day. Evidence for past overflow in the form of paleo-channels in the landscape is visible from satellite imagery. A step-wise increase in P of 25% was considered in all scenarios to simulate conditions at the onset of the AHP, in line with modelled estimates from Fischer et al. (2020). A 25% increase

in P is similar to previous estimates of increased rainfall during the AHP in other EARS lakes, such as paleo-Lake Suguta in Kenya (Borchardt and Trauth, 2012; Garcin et al., 2009; Junginger et al., 2014; Junginger and Trauth, 2013), and estimates across south-eastern equatorial Africa (20%) (Otto-Bliesner et al., 2014). For Scenarios 1 and 2 LCB reached 50% of its maximum volume (~40 km^3) by increasing the Segen River (S_i) and the Weyto River (W_i) discharge by 100% relative to modern day. Scenario 3 where LCB overflows into Lake Turkana, S_i and W_i were increased by 200% relative to modern day (Table 4).

Our model was run with an annual resolution for a period of 1,000 years, followed by 1,000 years of steady state conditions. This timescale was chosen to reflect the abrupt onset of the changes to hydroclimate observed in the AHP (Beck et al., 2019; Junginger and Trauth, 2013; Tierney and deMenocal, 2013; Trauth et al., 2018). A detailed description of prescribed inflow and outflow fluxes are in the methods section and initial conditions are given in Supplementary Table 1.

Table 4. Modelling lake scenarios for increased rainfall during the AHP.

Scenario	**Inflow from LC**	**Outflow to LT**	**ΔP (%)**	**ΔQ_{rivers} (%)**
1: Closed terminal LCB	N	N	+25	+100
2: Open terminal LCB	Y	N	+25	+100
3: Open flow-through LCB	Y	Y	+25	+200

4 Results

4.1 Stable isotopes $\delta^{18}O$ and $\delta^{2}H$

4.1.1 Rainfall

The rainfall stable isotope ($\delta^{18}O$ and $\delta^{2}H$) data from all Ethiopian stations in the Global Network of Isotopes in Precipitation (GNIP;

https://www.iaea.org/services/networks/gnip) was compiled. Addis Ababa is the only continuously-monitored GNIP station in Ethiopia (1961-2016 CE) at ~2400 m a.s.l., with high weighted mean rainfall $\delta^{18}O$ and $\delta^{2}H$ values of -1.28 ± 0.75‰ and +3.3 ± 5.7‰, respectively (Figure 3a). There are no rainfall isotope data for the lower elevation LCB region (~500 m a.s.l) therefore theoretical values for $\delta^{18}O$ (+1.6‰) and $\delta^{2}H$ (+24.0‰) were sourced from https://wateriso.utah.edu/waterisotopes/pages/data_access/form.html (Figure 3a).

4.1.2 Surface and sub-surface waters

The Weyto and Segen Rivers had mean $\delta^{18}O$ values of 0.2‰ (±0.5‰) and -0.7‰ (±1.26‰) and $\delta^{2}H$ values of 4.6‰ and 8.1‰, respectively. River $\delta^{18}O$ was positively offset from weighted mean rainfall by 0.5-1.5‰ and $\delta^{18}O$ values increased downstream (Figure 3b). The stable isotope values were similar to previously published data for MER rivers (Ayenew et al., 2008; Bretzler et al., 2011; Cockerton et al., 2013; Demlie et al., 2007a; Levin et al., 2009) and fell on a Local Evaporation Line with a slope of 4.50 (Figure 3b). Typically, MER river $\delta^{18}O$ is offset from weighted mean rainfall by +1-2‰ (Figure 3c), consistent with our results.

In contrast, average groundwater $\delta^{18}O$ from the LCB catchment was lower (-2.0‰, ±0.9‰) than weighed mean rainfall. Groundwaters from the upper Hammar Range group on the rift margins had the lowest $\delta^{18}O$ values (-2.5‰) whereas groundwaters sampled from the rift floor group (-1.4‰) and upper mixed group were higher (-1.2‰) (Figure 3d) and closer to weighted mean rainfall. This is consistent with previously measured groundwaters in the MER, which have the general trend of lower $\delta^{18}O$ values on the rift margins and higher values in the low elevation rift area.

4.1.3 Lakes

The average $\delta^{18}O$ values of LCB, Lake Chamo and Lake Abaya were 3.8‰, 5.4‰ and 5.6‰, respectively (Figure 3e). The higher $\delta^{18}O$ of lakes Chamo and Abaya, suggest higher evaporative conditions in these large, permanent lakes compared to LCB which is ephemeral. MER lake water $\delta^{18}O$ is typically offset compared to weighted mean rainfall (Figure 3c) by approximately +10‰, due to evaporative isotopic enrichment of lake waters. The evaporative enrichment of lakes Abaya, Chamo and LCB appear slightly lower than average with offsets between ~3-6‰.

4.2 Major anions and cations

The hydrochemistry of surface and groundwaters have not been characterised previously in the LCB basin so we provide a brief summary here. The major inflows to LCB, the Segen and Weyto Rivers are characterised by waters with a narrow pH range (7.98-8.74), low EC (<498 µS/cm), low TDS (<249 mg/l) and low total alkalinity (<178 mg/l). All hydro-geochemical data measured in this study are provided in the Supplementary (Supplementary Table 2, Figure 4). River waters haven no dominant cation, and anions are dominated by HCO_3^-. Low TDS, NO_3 (<1 mg/l) and PO_4 (<0.1 mg/l) (Supplementary Table 2), coupled with a lack of large-scale agriculture or industry suggests minimal anthropogenic input. LCB has higher concentrations of dissolved solids compared to riverine inputs (EC:750-780 µS/cm and TDS: 375-390 ppm; Supplementary Table 2) but had lower EC and TDS and was fresher than Lake Abaya and Lake Chamo (1044-1611 µS/cm and 522-806 ppm, respectively; Supplementary Table 2). The pH (7.99-7.49) and total alkalinity (306-339 mg/l) were also lower in LCB compared to the other lakes. LCB waters had no dominant cation, however anions were dominated in HCO_3^- (Supplementary Table 2), similar to riverine waters. Lake Abaya and Chamo displayed more characteristic ‘soda lake’ hydrochemistry as cations and anions were dominated in Na/K and HCO_3^-, respectively (Figure 4).

In the LCB basin, groundwaters typically have lower pH values (<7.62, Supplementary Table 2) compared to surface waters, but high EC (1,090-4,194 μS/cm) and TDS values (523-2,097 ppm), as high as an order of magnitude greater than surface waters. Group 1 groundwaters from the Upper Hammar Range rift margins of the LCB basin (CB18W5, CB18W6, CB18W13 and CB18W15; Figure 2) hydro-chemically cluster together but do not have a dominant cation or anion (Figure 4). Group 2 (Upper mixed) (CB18W17) and Group 3 (rift floor samples) (CB18W7 and CB18W10) groundwaters clustered together and cations were dominated in Na/K, similar to Lake Abaya and Lake Chamo. Anions were dominated by SO_4 and Cl (Figure 4).

4.3 Sr isotope geochemistry

4.3.1 Riverine and subsurface waters

Riverine Sr concentrations ranged from 137 to 349 ppb. Groundwaters consistently had higher Sr concentrations from 400 to 1,285 ppb, compared to riverine waters (Table S2, Figure 5). Riverine $^{87}Sr/^{86}Sr$ was low (relative to the modern seawater value of ~0.7091; (Spooner, 1976) and characteristic of waters draining young and non-radiogenic volcanic rocks (Figure 5). The range $^{87}Sr/^{86}Sr$ in Segen River waters was lower (0.7045-0.7070) than the Weyto (0.7061-0.7082). This trend is also reflected in the most evolved downstream waters of the main river channel just before the confluence point where the Segen and Weyto rivers join. Before the confluence point, the Weyto river water $^{87}Sr/^{86}Sr$ was more radiogenic (0.7061) than the Segen River (0.7055), despite the Segen catchment having a greater proportion of Precambrian basements rock with more radiogenic $^{87}Sr/^{86}Sr$ (Table 2).

Groundwaters had the most radiogenic $^{87}Sr/^{86}Sr$ signatures in this study, but were spatially variable. Group 1 groundwaters exhibited the highest $^{87}Sr/^{86}Sr$ with a range of 0.7080-0.7104 (Table S2, Figure 5). Group 2 groundwaters, in contrast, had a lower $^{87}Sr/^{86}Sr$ range (0.7042-0.7045), including a cold spring (0.7045). Group 3 low elevation rift floor

groundwaters had the lowest Sr concentrations. The $^{87}Sr/^{86}Sr$ values (0.7064) were in between the ranges of Group 1 and Group 2, and CB18W7 was similar to Weyto River waters.

4.3.2 Lakes

Lakes Abaya and Chamo (Figure 5) had low Sr concentrations (<140 ppb), similar to riverine waters in the LCB catchment, compared to LCB (~390 ppb). The average $^{87}Sr/^{86}Sr$ of lakes Chew Bahir, Chamo and Abaya were 0.7064, 0.7047 and 0.7062, respectively (Figure 5). LCB had the most radiogenic Sr lake waters, which were very similar to Group 3 groundwaters.

5 Discussion

5.1 LCB catchment dynamics

The dominant control on riverine trace element hydrochemistry is water-rock interactions from silicate weathering (Figure 6). Low Cl/Sr ratios relative to the marine value show enrichment in Sr with respect to Cl (Figure 7c). Further, the Na/Cl molar ratio is greater than unity for all riverine samples, suggesting Na excess relative to Cl (Figure 7b). Waters with Na/Cl molar ratios >1 may reflect more silicate weathering due to the reaction of feldspar minerals with carbonic acid present in water which releases HCO_3^- (Rajmohan and Elango, 2004) and the anions of all riverine and lake waters were dominated by HCO_3^- (Figure 4). Lake Abaya and Lake Chamo were dominated by Na/K cations, similar to Group 2 and 3 groundwaters (Figure 4).This is indicative of typical terminal soda lakes which accumulate high salt concentrations that are released via chemical weathering in the surrounding catchments and transferred as inflow via streams to form evaporating lake brines (Hardie et al., 1978). Typically, Ca and Mg reach saturation first, resulting in the precipitation of alkaline earth carbonates (Deocampo and Jones, 2014), whereas Na and K

remain in solution longer, subsequently increasing the pH (e.g. 9.10-9.13; Table S2) and alkalinity of the lake water. LCB in contrast is fresher suggesting shorter water residence times, which don't allow high salt concentrations to accumulate or active evaporite and carbonate precipitation on the lake floor. Lakes Chamo, Abaya and LCB fit with the hydrochemical range of previously reported MER lakes (Figure 4), are less fresh than Lakes Ziway, and Awassa, but not as evolved as Lake Shala or Lake Turkana, where dissolved solids may experience longer residence times.

Groundwaters were hydro-chemically distinct from surface waters with spatial trends within the catchment. Groundwater typically flows from the upper rift to the rift floor (JICA, 2012), where LCB acts as a semi-aquitard with limited flow from LCB towards Lake Turkana (Kebede et al., 2010a). Although groundwater has higher concentrations of dissolved solids relative to surface waters, this was unlikely due to evaporative concentration as groundwater stable water isotope ratios fall on the Global Meteoric Water Line, not an evaporation line. Isotopic values show an increasing trend with decreasing elevation which may reflect an altitudinal effect on $\delta^{18}O$ which is generally 0.5‰ km^{-1} for Ethiopian surface waters (Levin et al., 2009) and -0.9‰ km^{-1} for groundwaters (Haji et al., 2021). Group 1 groundwaters on the western elevated rift margins were dominated by water rock interactions, and moved towards more hydro-chemically evolved waters in the rift floor (Group 3) (Figure 6). During water-rock interaction multiple processes such as dissolution, precipitation, hydrolysis, ion exchange and oxidation-reduction reactions may imprint on the geochemical signature of groundwaters (Haji et al., 2021; Kebede et al., 2005). Group 1 Upper Hammer Range groundwaters were dominated by Ca/Mg cations and Group 2 and 3 groundwaters were Na/K dominated type (Figure 4) suggesting longer residence times, water-rock interaction and reverse weathering processes, typical of MER rift floor groundwaters (Kebede et al., 2005; Ayenew et al., 2008). Dissolution of evaporites or soil

salts such as trona or gypsum in alluvial aquifers could increase both SO_4 and Cl relative to surface waters, whilst ion exchange processes removing Ca and Mg from solution would cause a progressive reduction of Ca and Mg in solution further along groundwater flow paths.

5.2 Hydrological and lithological controls on $^{87}Sr/^{86}Sr$

The extreme differences in the $^{87}Sr/^{86}Sr$ of the two dominant lithologies in the EARS (Precambrian basement vs Cenozoic volcanics; Table 1) makes $^{87}Sr/^{86}Sr$ a useful hydrological tracer. It further permits reconstructions of paleo-$^{87}Sr/^{86}Sr$ from fossil carbonates to reveal changes in paleohydrology (Joordens et al., 2011; van der Lubbe et al., 2017). To determine whether LCB falls within the end-member $^{87}Sr/^{86}Sr$ inflow values, a three-component $^{87}Sr/^{86}Sr$ mixing model including average groundwater and riverine inputs from the Weyto and Segen rivers as an end-members is used (Figure 5). LCB falls within the end-member mixing zone, suggesting that groundwater and riverine flows can account for the range in LCB $^{87}Sr/^{86}Sr$. This mixing model also appears applicable to paleo LCB as it covers the range of $^{87}Sr/^{86}Sr$ measured in microfossils from LCB over the AHP (Junginger, unpublished data; van der Lubbe et al., 2017), supporting the use of our model to probe variations in $^{87}Sr/^{86}Sr$ resulting from Late Quaternary climate change. A similar mixing zone was created using a three-component mixing model for Lake Turkana based on previously published surface water $^{87}Sr/^{86}Sr$ data (van der Lubbe et al., 2017). Here, Lake Turkana falls slightly outside the theoretical mixing zone, which suggests a missing 'low' $^{87}Sr/^{86}Sr$ source. The mixing model for Turkana is based on limited point source information, which may be biased towards the season of sampling, and not representative of annual average inflows. Further, the Omo catchment, where >85% of Lake Turkana's inflows originate, has been influenced by a recent increase in anthropogenic activity over past decades. As Turkana is a larger lake system with longer response times, changes in Omo River $^{87}Sr/^{86}Sr$ from anthropogenic activity may not yet be apparent in Lake Turkana. Whilst anthropogenic

influences are difficult to rule out, the modern lake $^{87}Sr/^{86}Sr$ ratio of 0.7051 is similar to the most recently reported paleo-Turkana $^{87}Sr/^{86}Sr$ at 500 years BP (0.7050) and 2000 years BP (0.7051) (van der Lubbe, et al., 2017). Additionally, hydrothermal (e.g. Loiyangalani hot spring in the south-eastern Turkana catchment) variability in $^{87}Sr/^{86}Sr$ inflow may also act as an additional minor end-member for this lake system. Although beyond the scope of this study, further investigation is warranted to improve constraints on $^{87}Sr/^{86}Sr$ in paleo-Lake Turkana.

Segen and Weyto river $^{87}Sr/^{86}Sr$ values ranged from 0.7045 to 0.7070 and 0.7061 to 0.7082, respectively. Surprisingly, the Segen River waters overall were less radiogenic than the Weyto River, even though this catchment contains a larger proportion of Precambrian basement rocks (53 and 39%, respectively; Table 2) which have more radiogenic mean $^{87}Sr/^{86}Sr$ due to their older age and Rb/Sr ratios (Table 1). There was also disparity in surface lithology and lake water $^{87}Sr/^{86}Sr$ values in other catchments. The Chamo and Abaya catchments, which both have a small percentage surface cover comprised of older radiogenic bedrock (6 and 3%, respectively) and are dominated by Cenozoic volcanic and sedimentary deposits, had significantly different lake water $^{87}Sr/^{86}Sr$. Lake Chamo (0.7048) had a less radiogenic $^{87}Sr/^{86}Sr$ signature compared to Lake Abaya (0.7062), which was closer to the values of LCB (0.7064). This suggests that surface water $^{87}Sr/^{86}Sr$ is not solely controlled by the lithology.

Broadly, chemical weathering rates are largely controlled by the temperature and pressure at which the constituent minerals formed (Goldich, 1938), the specific surface area of mineral surfaces (West et al., 2005), climate (Meybeck, 1987; White and Brantley, 2003), and vegetation (Moulton et al., 2000). Although not discussed here in detail, tectonic activity is coupled to weathering rates by controlling the supply of fresh mineral surfaces and influencing global climate (Raymo et al., 1988). To investigate the relationship between

upstream lithology and surface water $^{87}Sr/^{86}Sr$, the lithology for the individual sample locations and catchment areas was calculated (apart from CB18W8 where a connection to the major river channel could not be established) (Table 2). Surface lithology was determined for major catchments (Chew Bahir, Abaya, Chamo and Turkana), sub-catchments (Weyto, Segen, Turkwel, Keiro and Omo) and within catchment samples, defined as the surface cover of the area upstream of the riverine sample points (Table 2). The predicted $^{87}Sr/^{86}Sr$ of catchment surface waters was corrected for the differences in weathering rates normalised to granite following W_{norm} values given in Bataille and Bowen (2012; see Table 2). Different weathering rates occur due to mineral surface areas and rock permeability and thus reactivity with aqueous solutions and account for the unequal contribution of bedrock lithologies to the dissolved Sr flux (Gibbs et al., 1999). There was a moderate correlation between measured $^{87}Sr/^{86}Sr$ and the proportions of Precambrian granitic/gneisses and Neogene/Paleogene volcanics in catchments (r^2 = 0.53 and 0.67, respectively; Figure 6). Quaternary sediments showed hardly any relationship which may reflect the fact that they represent an integrated mix of the catchment lithology, evaporites and potentially aeolian input.

The estimated $^{87}Sr/^{86}Sr$, based on upstream lithological surface cover, was in close agreement with measured values for Weyto and LCB catchments, where estimated values were slightly higher (0-0.004) than measured (Table 2). The estimated $^{87}Sr/^{86}Sr$ of Segen River catchment waters were also typically higher than measured, with greater variability on a tributary level, where the calculated values do not reflect the measured values in some parts of the catchment. For example, sample CB18W3 had 100% upstream surface cover comprising of Precambrian granitic/gneissic rocks however, the $^{87}Sr/^{86}Sr$ of the river water was unradiogenic (0.7045) suggesting a disconnect between apparent lithology and surface water $^{87}Sr/^{86}Sr$ in this part of the catchment. In all the other catchments, apart from the Turkwel, the estimated $^{87}Sr/^{86}Sr$ was lower than the measured values.

To account for the different weathering flux of lithological units, we introduced a relative weathering flux term (k). The use of a k value reduces these parameters into a single term whereby similar k values across catchments would suggest a single dominant control on weathering rates. The k value was solved by inverse modelling for each catchment utilising the measured $^{87}Sr/^{86}Sr$ values of catchments and the following equation:

$$R_{waterbody} = \frac{R_p(f_p \times Sr_p \times k_p)}{(f_p \times Sr_p \times k_p)+(f_q \times Sr_q \times k_q)+(f_n \times Sr_n \times k_n)} + \frac{R_n(f_n \times Sr_n \times k_n)}{(f_p \times Sr_p \times k_p)+(f_q \times Sr_q \times k_q)+(f_n \times Sr_n \times k_n)} + \frac{R_q(f_q \times Sr_q \times k_q)}{(f_p \times Sr_p \times k_p)+(f_q \times Sr_q \times k_q)+(f_n \times Sr_n \times k_n)} \quad (14)$$

where $R_{waterbody}$ is the Sr measured isotopic ratio of a given waterbody (e.g., LCB), R_x is the average Sr isotopic ratio of a given geological unit (denoted as *p:* Precambrian, *q*: Quaternary and *n*: Neogene/Paleogene; Table 1), f_x is the fraction of the catchment area covered by a given lithology, *Sr* is the Sr concentration of a given lithology, and k is the weathering flux of a given lithology. The k values are normalised relative to the granitic/gneissic Precambrian units (k_p = 1) (Table 2) and reflect the differences of Sr weathering fluxes between catchments.

There are clear differences in k values between catchments. The LCB catchment k values for each lithology are approximately one, suggesting catchment scale weathering congruency. However, LCB sub-catchments and the Turkwel, Omo, Abaya, Chamo, Turkana and Keiro catchments show a much wider variability in k values (0-4.3; Table 2). One explanation is the large range in Sr concentrations, $^{87}Sr/^{86}Sr$ ratios and age variability in Precambrian basement rock in the southern Ethiopian rift creating a large range in $^{87}Sr/^{86}Sr$ flux variability (Table 1) from the Precambrian basement. Another explanation is the contribution of dust and silt that are unrepresentative of the weathered rock in the catchment, transported via aeolian or alluvial processes, but contribute to the soil chemistry, such as volcanic ash.

At LCB, another potential explanation is the groundwater influence on rivers. The unexpectedly more radiogenic $^{87}Sr/^{86}Sr$ for the Weyto River samples relative to their surface geology may be explained in terms of groundwater input (baseflow). The role of groundwater for the maintenance of baseflow, particularly in rivers and wetlands, can be particularly important in water-limited semi-arid regions such as LCB (Baillie et al., 2007). In fact, it may be one of the most important low flow hydrological parameters in semi-arid regions (Mwakalila et al., 2002). The groundwaters sampled in the Weyto River basin were from Group 1 (Figure 2, Table 2), and have the most radiogenic $^{87}Sr/^{86}Sr$ (0.7080-0.7104) of all waters measured in this study (Table S2, Figure 5). These groundwaters were located in unconsolidated fluvial sediment aquifers overlying Precambrian granitic and gneissic rocks (Figure 6), the weathering of which was the likely dominant local source of the sediments in the dry wadi bed aquifers in this part of the catchment. There was only one groundwater sample in Group 2, as well as a cold spring. These groundwaters however have low $^{87}Sr/^{86}Sr$, suggesting a feature of the eastern rift flank may be less radiogenic $^{87}Sr/^{86}Sr$ (Figure 5). Although a better spatial coverage of groundwater is required to draw any firm conclusions, a less radiogenic groundwater baseflow component in the Segen catchment would provide an explanation for the lower Segen River $^{87}Sr/^{86}Sr$ observed, relative to the lithology which is comprised of more radiogenic rocks. It also would fit with the observation of weathering congruency at a catchment scale.

Groundwater inflow is also an end-member for LCB. Average $^{87}Sr/^{86}Sr$ of the riverine end-member input for LCB (combined Weyto and Segen) is less radiogenic than LCB lake water, requiring an additional end-member with more radiogenic $^{87}Sr/^{86}Sr$ for a mass balance. As average groundwaters have more radiogenic $^{87}Sr/^{86}Sr$, they likely represent an important end-member in the mass Sr balance of LCB. Further, the Group 3 groundwaters in the rift floor north of LCB although further along the ground water flowpath and likely more

evolved, are most similar in concentration and $^{87}Sr/^{86}Sr$ to riverine and LCB waters (Figure 5). We attribute this to the rift floor being a zone of surface-water-groundwater interaction, where mixing of riverine and groundwater occurs. Additionally, for a mass balance model of terminal LCB, a large proportion of surface inflows must be lost to groundwater recharge (Supplementary Table 1), and this likely occurs in the deltaic wetland region in the northern part of LCB.

5.3 Hydro-balance modelling of $^{87}Sr/^{86}Sr$ and $\delta^{18}O$

Sedimentary records from LCB provide evidence of wetter conditions during the AHP due to the distinct mineral assemblages in sediment layers which correspond to wet or dry phases (Foerster et al., 2018; Foerster et al., 2012; Foerster et al., 2015; Veihberg, et al., 2018). In the following sections we explore the role of hydrological re-organisation, subsequent impact on lake water $^{87}Sr/^{86}Sr$ and $\delta^{18}O$, modelled over Quaternary timescales and the potential of combined $^{87}Sr/^{86}Sr$ and $\delta^{18}O$ in paleo lacustrine carbonates as a proxy of catchment size and interconnectivity. Lake hydro-balance modelling (Figure 8) allowed us to explore changes in the isotopic composition of LCB over three scenarios at the onset of the AHP, assuming a 25% precipitation increase (see Section 3.3): (1) Closed terminal LCB, (2) Open terminal LCB, and (3) Open flow-through LCB (Table 4). The percentage of dissolved Sr delivered to LCB from each end-member (Weyto River, groundwater etc.), including the percentage of buffering from stored Sr in LCB, is shown in Figure 8c at the start and end of the modelling period. In all scenarios, the initial $\delta^{18}O$ and $^{87}Sr/^{86}Sr$ of LCB was +3.8‰ and 0.7064, respectively, to reflect modern values (Supplementary Table 2). The theoretical water residence times based on the Sr concentrations of the maximum volume closed LCB (Figure 9a) and flow-through LCB (Figure 9b) were also calculated following Yuretich and Cerling (1983):

$$\tau_i = \frac{V_{lake} \times Mi}{Mi(V_{GW}+V_{overflow})} \quad (15)$$

where τ is the annual residence time of the solute *i*, *Mi* is the amount of solute *i* in the water body, V_{lake} is the lake volume and the annual flux of the solute leaving the water body via groundwater recharge (V_{GW}) and overflow to Turkana ($V_{overflow}$) assuming ideal conditions with a well-mixed, unstratified lake. Overflow to Lake Turkana is initiated once the overflow threshold is surpassed, using the output from the lake balance modelling. Under modern closed-lake conditions, Sr residence times are <1 year and are more sensitive to changes in Sr influxes.

5.3.1 Scenario 1: Closed terminal Lake Chew Bahir

Under closed-lake conditions, modelled $^{87}Sr/^{86}Sr$ decreased from 0.7064 to 0.7062 (Figure 8a), and $\delta^{18}O$ increased to ~11‰ by model year 2000. This suggests a large range (~10‰) in $\delta^{18}O$, is possible due to intra-catchment dynamics alone, i.e. no inter-catchment connectivity. The increase in $\delta^{18}O$ reflects the enhanced influence of evaporation in an expanding semi-arid lake and is within the range of $\delta^{18}O$ reported in modern day MER lakes (Figure 3e). The decrease in $^{87}Sr/^{86}Sr$ is directly related to increased surface inflow with less radiogenic $^{87}Sr/^{86}Sr$, and occurs directly in phase with linear increases in inflows.

5.3.2 Scenario 2: Open terminal Lake Chew Bahir

Another scenario during the AHP is hydrological reorganisation which includes additional inflow from Lake Chamo via the Segen River, which infrequently occurs under modern conditions when precipitation exceeds the long term average. Interestingly, although the inflow from Lake Chamo resulted in a larger lake than in Scenario 1 (Figure 8b), $^{87}Sr/^{86}Sr$ was only slightly lower (~0.0003) and $\delta^{18}O$ 1‰ higher. Overflow from Lake Chamo into LCB is unlikely a major driver in changes in lake water chemistry.

5.3.3 Scenario 3: Open Flow-through Lake Chew Bahir

The third scenario considered was an inter-connected lake system, where LCB overflows and creates a large N-S cascading lake system connecting Lake Abaya, Lake Chamo, LCB and finally Lake Turkana. The $\delta^{18}O$ change over the modelled period was significantly different in this scenario. $\delta^{18}O$ increased over the modelling period, similar to other scenarios, until the overflow point was surpassed and discharge was initiated to Lake Turkana. At this point $\delta^{18}O$ rapidly decreases from ~11‰, stabilising at 8‰ when steady state conditions begin at model year 1000. Under humid conditions when LCB became a flow-through system, $\delta^{18}O$ is still likely to be high, but trending towards lower values than other scenarios by up to 3‰. This is consistent with $\delta^{18}O$ reconstructions of ostracods from outcrops at Lake Turkana, where a 1.5‰ decrease occurred in the fossil record during phases of overflow and connectivity to the White Nile (Beck et al., 2019). Our modelling suggests that the transition from terminal to flow-through lake conditions in lake systems like LCB, may be even more pronounced.

Modelled $^{87}Sr/^{86}Sr$ in LCB also changed significantly in this scenario from 0.7064 to ~0.7061, which is greater in magnitude than the change in the terminal LCB scenarios (Figure 8). This suggests that the greatest change in $^{87}Sr/^{86}Sr$ occurs via a transition from smaller terminal lake to a large flow-through lake. A decrease in the residence times of dissolved Sr (~30 years to 20 years) occurred after LCB switched to a flow-through system, increasing the lake's sensitivity to changes in surface water inflows (Figure 9b).

5.4 Lake water $\delta^{18}O$ change at the AHP onset

Dynamic changes in lake water $\delta^{18}O$ have been reported in the endogenic calcite record from LCB lake cores with a range of +0.5 to +9.0 ‰ (VPDB) over the AHP (Viehberg, et al., 2018). Once converted to the VSMOW scale (Coplen et al., 1998), assuming temperature dependent fractionation between water and calcite (Kim and O'Neil, 1997) and a modern lake water temperature of ~30.5 °C, we estimate that lake water ranged from +4.0 to +12.6‰

(VSMOW) at the onset of the AHP period. Lake water $\delta^{18}O$ is sensitive to two main factors; 1) the degree of evaporative fractionation and 2) the $\delta^{18}O$ of the precipitation moisture source (Leng and Marshall, 2004). The latter may vary with changes in the strength of the East African Monsoon or West African Monsoon (Viehberg et al., 2018), bringing rainfall from the Atlantic or Indian Ocean, respectively. Lake water $\delta^{18}O$ in our model simulations, driven by a constant $\delta^{18}O$ precipitation input, ranged from +1.0 to +11.5‰ and are comparable to the paleorecord, suggesting evaporation is the fundamental control on $\delta^{18}O$ at semi-arid LCB. Our results may also offer an alternative interpretation of paleolake-$\delta^{18}O$. In our modelled results the lowest $\delta^{18}O$ values occurred when LCB was a smaller lake system, namely due to shorter lake water residence times (Figure 9a) and the higher ratio of groundwater (with lower $\delta^{18}O$) to surface water inflows (Figure 10). Conversely, the highest modelled $\delta^{18}O$ values occurred when LCB was a closed lake system. Connectivity to Turkana resulted in a decreasing trend in $\delta^{18}O$. However, $\delta^{18}O$ was within the range of closed basin values, meaning it would be difficult to suggest open versus closed lake conditions based on the $\delta^{18}O$ proxy alone, but in combination with $^{87}Sr/^{86}Sr$, trends in lake levels may be interpretable.

5.5 Lake water $^{87}Sr/^{86}Sr$ change at the AHP onset

Scenarios 1 and 2 cover approximately half the variability of $^{87}Sr/^{86}Sr$ derived from measurements of carbonate microfossil material at LCB over the AHP (0.7065-0.7060; van der Lubbe et al., 2017; Junginger et al., unpublished data). The third scenario, where LCB overflowed to Lake Turkana, showed the greatest $^{87}Sr/^{86}Sr$ range. Sustained connectivity to Lake Turkana creates an extra outflow of Sr from LCB, effectively flushing Sr until a new steady state is reached. Consequently, Sr residence times for the open flow-through LCB scenario are lower (<20 years) (Figure 9b).

Our maximum lake water residence times of ~35 years suggest a dynamic lake system which could respond quickly to changes in Sr influxes (i.e. being cut off from surface inflows). This is in contrast to the record from Lake Turkana, which shows smooth and gradual changes in $^{87}Sr/^{86}Sr$ over the AHP, most likely due to the larger buffering capacity of this sizeable lake (~200 times larger than LCB at present day). Dissolution of lake basin evaporites, formed from past water pulses and subsequent evaporation episodes, could also provide an additional source of Sr during lake-filling episodes, the influence of which is difficult to account for. This could lag the response time of lake water $^{87}Sr/^{86}Sr$ to hydrological reorganisation. For example, if we consider the most extreme example of the complete desiccation of the maximum volume of LCB where 100% of the Sr in the water is precipitated as evaporites on the lake basin floor, we can suggest a potential upper limit of this process. Based on modern lake concentrations of Sr (394 ppb) and a maximum surface volume of ~83 km^3 an additional 3.3 x 10^7 kg of Sr would be released into LCB during filling episodes. This would effectively act as an additional inflow of 'recycled' Sr with the $^{87}Sr/^{86}Sr$ of past lake water to the lake water budget. If we assume this is released at a constant rate during lake filling this could represent a maximum of 0.1 to 4% of the total Sr input on an annual time step. In reality, not all lake Sr would be converted to surface evaporites and a proportion would be removed as groundwater recharge and depending time interval separating lake filling episodes evaporites may also buried via sedimentation processes estimated at 0.1-1.3 mm a^{-1} (Foerster et al., 2012).

5.6 Sensitivity analysis for the surface-water-to-groundwater ratio

The larger range of $^{87}Sr/^{86}Sr$ (0.7065 to 0.7060) measured in microfossils from LCB (van der Lubbe et al., 2017) could not be simulated by our model (~0.7064-0.7061) considering only changes in catchment connectivity. Our hydro-balance shows that the modern ratio of surface water and groundwater inputs based on discharge ($R_{Q,sw/gw}$) is 11:1,

however, when considering the much higher Sr concentrations in groundwaters compared to surface waters (Table S2), i.e. the Sr flux ratio of surface waters to groundwaters ($R_{Sr,sw/gw}$) is much lower at 4:1. In our model simulations groundwater input was held constant, and in Figure 10 the sensitivity of the LCB system to changes in this ratio is shown. For example, more radiogenic $^{87}Sr/^{86}Sr$ may be explained by an increase in groundwater discharge into LCB due to rising water tables. Lower $^{87}Sr/^{86}Sr$ during the AHP may be explained by reduced groundwater inflow relative to today (higher $R_{Q,sw/gw}$). Large changes in precipitation will also result in changes to the water table, however groundwater response times are typically slow (e.g. estimated at 100-1000 years in Olduvai gorge, Tanzania, (Cuthbert et al., 2017)) compared to runoff and out of step with meteorological and surface hydrological change (Cuthbert et al., 2019). Furthermore, during lake desiccation episodes, groundwater inflow (discharge) may also have played an important buffering role maintaining higher lake levels in a drying climate and allowing groundwater refugia to develop (Cuthbert et al., 2017). Therefore, groundwater inflow may buffer surface inflows to varying degrees, which should be reflected by changes in $^{87}Sr/^{86}Sr$. Whilst beyond the scope of this study, an improved understanding of groundwater flow dynamics and age in southern Ethiopia would be invaluable for improving paleo climatic reconstructions using $^{87}Sr/^{86}Sr$.

6 Conclusions

Our study provides the first known major hydrochemical investigation of the Lake Chew Bahir catchment in southern Ethiopia. The major, trace, and Sr and O isotopic composition of surface and groundwaters reported in this study are within the range of previously published data in the EARS, suggesting the LCB catchment is a good analogue for other semi-arid catchments in the region. Groundwater-surface water interactions at terminal, semi-arid LCB plays a significant role in water hydrochemistry. The Sr mass balance of LCB cannot be achieved by only including surface water inflows, or explain the modern lake water

$^{87}Sr/^{86}Sr$ ratios. This demonstrates the important role of groundwater in dryland lake basins and supports the hypothesis that perennial springs likely play a central buffering role in sustaining water supplies in areas which typically experience climatically induced large-scale surface water fluctuations (Cuthbert et al., 2019).

LCB has short (20-35 years) Sr residence times based on model simulations. $\delta^{18}O$ is sensitive to the evaporative conditions and lake water residence times. Higher $\delta^{18}O$ is likely indicative of a larger closed-lake system. Lake $\delta^{18}O$ values greater than 8‰ suggest a closed lake system, whereas a decreasing trend in $\delta^{18}O$ indicates a flow-through lake and subsequent connectivity to Lake Turkana. Coupled low $^{87}Sr/^{86}Sr$ and high $\delta^{18}O$ would suggest large-scale hydrological reorganisation, able to support a flow-through lake system where the Sr budget was dominated by surface inflows. Isotopic data from microfossils could provide key insights on paleo-hydrological connectivity between LCB and Lake Turkana and allow time periods of cascading lake systems to be identified. Conversely, periods dominated and buffered by groundwater inflows indicated by lower $\delta^{18}O$ and higher $^{87}Sr/^{86}Sr$ may also be readily identified. This likely played an integral role in the availability of freshwater resources for our human ancestors in the region during documented climatic instability over the Quaternary (Viehberg et al., 2018; Foerster et al., 2018). The combined use of $^{87}Sr/^{86}Sr$ and $\delta^{18}O$ can provide important insights to change in hydroclimate in southern Ethiopia.

References

Alcalá, F.J., Custodio, E., 2008. Using the Cl/Br ratio as a tracer to identify the origin of salinity in aquifers in Spain and Portugal. Journal of Hydrology 359, 189-207.

Asrat, A., Barbey, P., Gleizes, G., 2001. The Precambrian Geology of Ethiopia: a review. Africa Geosciences Review 8, 271-288.

Asrat, A., Barbey, P., 2003. Petrology, geochronology and Sr-Nd isotopic geochemistry of the Konso pluton, South-western Ethiopia: implications for transition from convergence to extension in the Mozambique Belt. International Journal of Earth Sciences 92, 873-890.

Ayenew, T., Kebede, S., Alemyahu, T., 2008. Environmental isotopes and hydrochemical study applied to surface water and groundwater interaction in the Awash River basin. Hydrological Processes 22, 1548-1563.

Baddouh, M.b., Meyers, S.R., Carroll, A.R., Beard, B.L., Johnson, C.M., 2016. Lacustrine 87Sr/86Sr as a tracer to reconstruct Milankovitch forcing of the Eocene hydrologic cycle. Earth and Planetary Science Letters 448, 62-68.

Baillie, M.N., Hogan, J.F., Ekwurzel, B., Wahi, A.K., Eastoe, C.J., 2007. Quantifying water sources to a semiarid riparian ecosystem, San Pedro River, Arizona. Journal of Geophysical Research: Biogeosciences 112.

Bataille, C.P., Bowen, G.J., 2012. Mapping 87Sr/86Sr variations in bedrock and water for large scale provenance studies. Chemical Geology 304-305, 39-52.

Beck, C.C., Feibel, C.S., Wright, J.D., Mortlock, R.A., 2019. Onset of the African Humid Period by 13.9 kyr BP at Kabua Gorge, Turkana Basin, Kenya. The Holocene 29, 1011-1019.

Belete, A., Beccaluva, L., Bianchini, G., Colombani, N., Fazzini, M., Marchina, C., Natali, C., Rango, T., 2015. Water–Rock Interaction and Lake Hydrochemistry in the Main Ethiopian Rift, in: Billi, P. (Ed.), Landscapes and Landforms of Ethiopia. Springer Netherlands, Dordrecht, pp. 307-321.

Bloszies, C., Forman, S.L., Wright, D.K., 2015. Water level history for Lake Turkana, Kenya in the past 15,000years and a variable transition from the African Humid Period to Holocene aridity. Global and Planetary Change 132, 64-76.

Bonini, M., Corti, G., Innocenti, F., Manetti, P., Mazzarini, F., Abebe, T., Pecskay, Z., 2005. Evolution of the Main Ethiopian Rift in the frame of Afar and Kenya rifts propagation. Tectonics 24.

Borchardt, S., Trauth, M.H., 2012. Remotely-sensed evapotranspiration estimates for an improved hydrological modeling of the early Holocene mega-lake Suguta, northern Kenya Rift. Palaeogeography, Palaeoclimatology, Palaeoecology 361-362, 14-20.

Bretzler, A., Osenbrück, K., Gloaguen, R., Ruprecht, J.S., Kebede, S., Stadler, S., 2011. Groundwater origin and flow dynamics in active rift systems – A multi-isotope approach in the Main Ethiopian Rift. Journal of Hydrology 402, 274-289.

Chamberlain, C.P., Wan, X., Graham, S.A., Carroll, A.R., Doebbert, A.C., Sageman, B.B., Blisniuk, P., Kent-Corson, M.L., Wang, Z., Chengshan, W., 2013. Stable isotopic evidence for climate and basin evolution of the Late Cretaceous Songliao basin, China. Palaeogeography, Palaeoclimatology, Palaeoecology 385, 106-124.

Clement, J., Caroff, M., Hemond, C., Tiercelin, J., Bollinger, C., Guillou, H., Cotten, J., 2003. Pleistocene magmatism in a lithospheric transition area: petrogenesis of alkaline and peralkaline lavas from the Baringo-Bogoria Basin. Canadian Journal of Earth Sciences 40: 9, 1239-1257.

Cockerton, H.E., Street-Perrott, F.A., Leng, M.J., Barker, P.A., Horstwood, M.S.A., Pashley, V., 2013. Stable-isotope (H, O, and Si) evidence for seasonal variations in hydrology and Si cycling from modern waters in the Nile Basin: implications for interpreting the Quaternary record. Quaternary Science Reviews 66, 4-21.

Coplen, T.B., 1996. New guidelines for reporting stable hydrogen, carbon, and oxygen isotope-ratio data. Geochimica et Cosmochimica Acta 60, 3359-3360.

Cohen, A., Talbot, M.R., Awramik, S.M., Dettman, D.L., Abell, P., 1997. Lake level and paleoenvironmental history of Lake Tanganyika, Africa, as inferred from late Holocene and modern stromatolites.

Craig, H., Gordon, L.I., 1965. Deuterium and oxygen-18 variations in the ocean and the marine atmospher, Proceedings of a Conference on Stable Isotopes in Oceanographic Studies and Paleotemperatures, Spoleto, Italy, pp. 9-130.

Cuthbert, M.O., Gleeson, T., Moosdorf, N., Befus, K.M., Schneider, A., Hartmann, J., Lehner, B., 2019. Global patterns and dynamics of climate–groundwater interactions. Nature Climate Change 9, 137-141.

Cuthbert, M.O., Gleeson, T., Reynolds, S.C., Bennett, M.R., Newton, A.C., McCormack, C.J., Ashley, G.M., 2017. Modelling the role of groundwater hydro-refugia in East African hominin evolution and dispersal. Nature Communications 8, 15696.

Darling, W.G., Gizaw, B., Arusei, M.K., 1996. Lake-groundwater relationships and fluid-rock interaction in the East African Rift Valley: isotopic evidence. Journal of African Earth Sciences 22, 423-431.

Demlie, M., Ayenew, T., Wohnlich, S., 2007a. Comprehensive hydrological and hydrogeological study of topographically closed lakes in highland Ethiopia: The case of Hayq and Ardibo. Journal of Hydrology 339, 145-158.
Demlie, M., Wohnlich, S., Gizaw, B., Stichler, W., 2007b. Groundwater recharge in the Akaki catchment, central Ethiopia: evidence from environmental isotopes (δ18O, δ2H and 3H) and chloride mass balance. Hydrological Processes 21, 807-818.
Deocampo, D.M., Jones, B.F., 2014. 7.13 - Geochemistry of Saline Lakes, in: Holland, H.D., Turekian, K.K. (Eds.), Treatise on Geochemistry (Second Edition). Elsevier, Oxford, pp. 437-469.
Dettman, D.L., Palacios-Fest, M.R., Nkotagu, H.H., Cohen, A.S., 2005. Paleolimnological investigations of anthropogenic environmental change in Lake Tanganyika: VII. Carbonate isotope geochemistry as a record of riverine runoff. Journal of Paleolimnology 34, 93-105.
Doebbert, A.C., Johnson, C.M., Carroll, A.R., Beard, B.L., Pietras, J.T., Rhodes Carson, M., Norsted, B., Throckmorton, L.A., 2014. Controls on Sr isotopic evolution in lacustrine systems: Eocene green river formation, Wyoming. Chemical Geology 380, 172-189.
Fischer, M.L., Markowska, M., Bachofer, F., Foerster, V.E., Asrat, A., Zielhofer, C., Trauth, M.H., Junginger, A., 2020. Determining the Pace and Magnitude of Lake Level Changes in Southern Ethiopia Over the Last 20,000 Years Using Lake Balance Modeling and SEBAL. Frontiers in Earth Science 8.
Foerster, V., Deocampo, D.M., Asrat, A., Günter, C., Junginger, A., Krämer, K.H., Stroncik, N.A., Trauth, M.H., 2018. Towards an understanding of climate proxy formation in the Chew Bahir basin, southern Ethiopian Rift. Palaeogeography, Palaeoclimatology, Palaeoecology 501, 111-123.
Foerster, V., Junginger, A., Langkamp, O., Gebru, T., Asrat, A., Umer, M., Lamb, H.F., Wennrich, V., Rethemeyer, J., Nowaczyk, N., Trauth, M.H., Schaebitz, F., 2012. Climatic change recorded in the sediments of the Chew Bahir basin, southern Ethiopia, during the last 45,000 years. Quaternary International 274, 25-37.
Foerster, V., Vogelsang, R., Junginger, A., Asrat, A., Lamb, H.F., Schaebitz, F., Trauth, M.H., 2015. Environmental change and human occupation of southern Ethiopia and northern Kenya during the last 20,000 years. Quaternary Science Reviews 129, 333-340.
Fontes, J.-C., Maglione, G., Roche, M.-A., 1970. Eléments d'hydrologie isotopique dans le bassin du lac Tchad. International atomic energy, Vienna, 209-219.
Forman, S.L., Wright, D.K., Bloszies, C., 2014. Variations in water level for Lake Turkana in the past 8500 years near Mt. Porr, Kenya and the transition from the African Humid Period to Holocene aridity. Quaternary Science Reviews 97, 84-101.
Furi, W., Razack, M., Abiye, T.A., Kebede, S., Legesse, D., 2012. Hydrochemical characterization of complex volcanic aquifers in a continental rifted zone: the Middle Awash basin, Ethiopia. Hydrogeology Journal 20, 385-400.
Furman, T., Kalet, K.M., Bryce, J.G., Hanan, B.B., Tertiary Mafic Lavas of Turkana, Kenya: Constraints on East African Plume Structure and the Occurrence of High-μ Volcanism in Africa. Journal of Petrology 47, 1221-1244.
Garcin, Y., Junginger, A., Melnick, D., Olago, D.O., Strecker, M.R., Trauth, M.H., 2009. Late Pleistocene–Holocene rise and collapse of Lake Suguta, northern Kenya Rift. Quaternary Science Reviews 28, 911-925.
Gat, J.R., 1996. Oxygen anf hydrogen isotopes in the hydrologic cycle. Annual Review of Earth and Planetary Sciences 24, 225-262.
George, R., Rogers, N., 2002. Plume dynamics beneath the African plate inferred from the geochemistry of the Tertiary basalts of southern Ethiopia. Contributions to Mineralogy and Petrology 144, 286-304.
Gibbs, M.T., Bluth, G.J.S., Fawcett, P.J., Kump, L.R., 1999. Global chemical erosion over the last 250 my; variations due to changes in paleogeography, paleoclimate, and paleogeology. American Journal of Science 299, 611-651.
Gibson, J.J., Birks, S.J., Yi, Y., 2016. Stable isotope mass balance of lakes: a contemporary perspective. Quaternary Science Reviews 131, 316-328.
Gibson, J.J., Edwards, T.W.D., 2002. Regional water balance trends and evaporation-transpiration partitioning from a stable isotope survey of lakes in northern Canada. Global Biogeochemical Cycles 16, 10-11-10-14.
Gizaw, B., 2002. Hydrochemical and environmental investigation of the Addis Ababa region, Ethiopia. Unpublished PhD Thesis, Ludwig Macmillan, University of Munich, Munich.
Goldich, S.S., 1938. A Study in Rock-Weathering. The Journal of Geology 46, 17-58.
Golubtsov, A.S., Habteselassie, R., 2010. Fish faunas of the Chamo-Abaya and Chew Bahir basins in southern portion of the Ethiopian Rift Valley: origin and prospects for survival. Aquatic Ecosystem Health & Management 13, 47-55.
Gonfiantini, R., 1986. Chapter 3 – Environmental isotopes in lake studies A2 - Fritz, P., in: Fontes, J.C. (Ed.), The Terrestrial Environment, B. Elsevier, Amsterdam, pp. 113-168.
Gonfiantini, R., Borsi, S., Ferrara, G., Panichi, C., 1973. Isotopic composition of waters from the Danakil depression (Ethiopia). Earth and Planetary Science Letters 18, 13-21.

Grove, A., Street, A. and Goudie, A., 1975. Former Lake Levels and Climatic Change in the Rift Valley of Southern Ethiopia, The Geographical Journal 141, 177–194.
Haji, M., Qin, D., Guo, Y., Li, L., Wang, D., Karuppannan, S., Shube, H., 2021. Origin and geochemical evolution of groundwater in the Abaya Chamo basin of the Main Ethiopian Rift: application of multi-tracer approaches. Hydrogeology Journal.
Halcrow. 2008. Rift Valley Lakes Basin Integrated Resources Development Master Plan Study Project, Draft Phase 2 Report Part II Prefeasibility Studies, Halcrow Group Limited, and Generation Integrated Rural Development (GIRD) Consultants Unpublished report. Addis Ababa.
Hardie, L.A., Smoot, J.P., Eugster, H.P., 1978. Saline lakes and their deposits:a sedimentological approach, in: Matter, A., Tucker, M.E. (Eds.), Modern and Ancient Lake Sediments. Blackwell Scientific Publications, Oxford, pp. 7-42.
Hart, W.S., Quade, J., Madsen, D.B., Kaufman, D.S., Oviatt, C.G., 2004. The 87Sr/86Sr ratios of lacustrine carbonates and lake-level history of the Bonneville paleolake system. Geological Society of America Bulletin 116, 1107-1119.
Horita, J., Rozanski, K., Cohen, S., 2008. Isotope effects in the evaporation of water: a status report of the Craig–Gordon model. Isotopes in Environmental and Health Studies 44, 23-49.
Horita, J., Wesolowski, D.J., 1994. Liquid-vapor fractionation of oxygen and hydrogen isotopes of water from the freezing to the critical temperature. Geochimica et Cosmochimica Acta 58, 3425-3437.
IAEA, 2019. Global Network of Isotopes in Rivers. The GNIR Database. Accessed 07.02.2020 [http://www-naweb.iaea.org/napc/ih/IHS_resources_isohis.html]
Janzen, A., Bataille, C., Copeland, S.R., Quinn, R.L., Ambrose, S.H., Reed, D., Hamilton, M., Grimes, V., Richards, M.P., le Roux, P., Roberts, P., 2020. Spatial variation in bioavailable strontium isotope ratios (87Sr/86Sr) in Kenya and northern Tanzania: Implications for ecology, paleoanthropology, and archaeology. Palaeogeography, Palaeoclimatology, Palaeoecology 560, 109957.
JICA. 2012. The Study on Groundwater Resources Assessment in the Rift Valley Lakes Basin in Ethiopia Final Report (Main Report), JICA, Kokusai Kogyo Co., Ltd., MoWE, Ethiopia.
Johnson, T.C., Malala, J.O., 2009. Lake Turkana and Its Link to the Nile, in: Dumont, H.J. (Ed.), The Nile: Origin, Environments, Limnology and Human Use. Springer Netherlands, Dordrecht, pp. 287-304.
Jones, M.D., Cuthbert, M.O., Leng, M.J., McGowan, S., Mariethoz, G., Arrowsmith, C., Sloane, H.J., Humphrey, K.K., Cross, I., 2016. Comparisons of observed and modelled lake $\delta^{18}O$ variability. Quaternary Science Reviews 131, 329-340.
Joordens, J.C.A., Vonhof, H.B., Feibel, C.S., Lourens, L.J., Dupont-Nivet, G., van der Lubbe, J.H.J.L., Sier, M.J., Davies, G.R., Kroon, D., 2011. An astronomically-tuned climate framework for hominins in the Turkana Basin. Earth and Planetary Science Letters 307, 1-8.
Junginger, A., Roller, S., Olaka, L.A., Trauth, M.H., 2014. The effects of solar irradiation changes on the migration of the Congo Air Boundary and water levels of paleo-Lake Suguta, Northern Kenya Rift, during the African Humid Period (15–5ka BP). Palaeogeography, Palaeoclimatology, Palaeoecology 396, 1-16.
Junginger, A., Trauth, M.H., 2013. Hydrological constraints of paleo-Lake Suguta in the Northern Kenya Rift during the African Humid Period (15–5kaBP). Global and Planetary Change 111, 174-188.
Kebede, E., Mariam, Z.G., Ahlgren, I., 1994. The Ethiopian Rift Valley lakes: chemical characteristics of a salinity-alkalinity series. Hydrobiologia 288, 1-12.
Kebede, S., 2004. Environmental isotopes and geochemistry in investigating groundwater and lake hydrology: cases from the Blue Nile basin & the Ethiopian Rift (Ethiopia) Hydrogeology. Université d'Avignon et des Pays de Vaucluse d'Avignon, p. 162.
Kebede, S., Ketema, A., Tesema, Z., 2010a. Features of groundwaters in basins shared between Ethiopia and Kenya and the implications for international legislation on transboundary aquifers. Hydrogeology Journal 18, 1685-1697.
Kebede, S., Travi, Y., Alemayehu, T., Ayenew, T., 2005. Groundwater recharge, circulation and geochemical evolution in the source region of the Blue Nile River, Ethiopia. Applied Geochemistry 20, 1658-1676.
Kebede, S., Travi, Y., Asrat, A., Alemayehu, T., Ayenew, T., Tessema, Z., 2007. Groundwater origin and flow along selected transects in Ethiopian rift volcanic aquifers. Hydrogeology Journal 16, 55.
Kebede, S., Travi, Y., Rozanski, K., 2009. The $\delta^{18}O$ and $\delta^{2}H$ enrichment of Ethiopian lakes. Journal of Hydrology 365, 173-182.
Kebede, S., Travi, Y., Stadler, S., 2010b. Groundwaters of the Central Ethiopian Rift: diagnostic trends in trace elements, $\delta^{18}O$ and major elements. Environmental Earth Sciences 61, 1641-1655.
Kebede, S.A., Tenalem; Umer,Mohammed, 2001. Application of isotope and water balance approaches for the study of the hydrogeological regime of the Bishoftu crater lakes, Ethiopia. Ethiopian Journal of Science 24, 151-166.

Kebede, T., Koeberl, C., 2003. Petrogenesis of A-type granitoids from the Wallagga area, western Ethiopia: constraints from mineralogy, bulk-rock chemistry, Nd and Sr isotopic compositions. Precambrian Research 121, 1-24
Kebede, T., Koeberl, C., Koller, F., 1999. Geology, geochemistry and petrogenesis of intrusive rocks of the Wallagga area, western Ethiopia. Journal of African Earth Sciences 29, 715-734.
Coplen, T.B., 1996. New guidelines for reporting stable hydrogen, carbon, and oxygen isotope-ratio data. Geochimica et Cosmochimica Acta 60, 3359-3360.
Kim, S.-T., Mucci, A., Taylor, B.E., 2007. Phosphoric acid fractionation factors for calcite and aragonite between 25 and 75 °C: Revisited. Chemical Geology 246, 135-146.
Leng, M.J., Lamb, A.L., Lamb, H.F., Telford, R.J., 1999. Palaeoclimatic implications of isotopic data from modern and early Holocene shells of the freshwater snail Melanoides tuberculata, from lakes in the Ethiopian Rift Valley. Journal of Paleolimnology 21, 97-106.
Leng, M.J., Marshall, J.D., 2004. Palaeoclimate interpretation of stable isotope data from lake sediment archives. Quaternary Science Reviews 23, 811-831.
Levin, N.E., Zipser, E.J., Cerling, T.E., 2009. Isotopic composition of waters from Ethiopia and Kenya: Insights into moisture sources for eastern Africa. Journal of Geophysical Research: Atmospheres 114.
Lowenstein, T.K., Risacher, F., 2009. Closed Basin Brine Evolution and the Influence of Ca–Cl Inflow Waters: Death Valley and Bristol Dry Lake California, Qaidam Basin, China, and Salar de Atacama, Chile. Aquatic Geochemistry 15, 71-94.
McKenzie, J.M., Siegel, D.I., Patterson, W., McKenzie, D.J., 2001. A geochemical survey of spring water from the main Ethiopian rift valley, southern Ethiopia: implications for well-head protection. Hydrogeology Journal 9, 265-272.
Mechal, A., Birk, S., Dietzel, M., Leis, A., Winkler, G., Mogessie, A., Kebede, S., 2017. Groundwater flow dynamics in the complex aquifer system of Gidabo River Basin (Ethiopian Rift): a multi-proxy approach. Hydrogeology Journal 25, 519-538.
Meshesha, D., Shinjo, R., Matsumura, R., Chekol, T., 2011. Metasomatized lithospheric mantle beneath Turkana depression in southern Ethiopia (the East Africa Rift): geochemical and Sr–Nd–Pb isotopic characteristics. Contributions to Mineralogy and Petrology 162, 889-907.
Meybeck, M., 1987. Global chemical weathering of surficial rocks estimated from river dissolved loads. American Journal of Science 287, 401-428.
Moulton, K.L., West, J., Berner, R.A., 2000. Solute flux and mineral mass balance approaches to the quantification of plant effects on silicate weathering. American Journal of Science 300, 539-570.
Mwakalila, S., Feyen, J., Wyseure, G., 2002. The influence of physical catchment properties on baseflow in semi-arid environments. Journal of Arid Environments 52, 245-258.
OCHA, 2020. Eastern Africa Region: Floods and locust outbreak snapshot. United Nations Office for the Coordination of Humanitarian Affairs. Accessed 01.02.2021 [https://reliefweb.int/report/ethiopia/eastern-africa-region-floods-and-locust-outbreak-snapshot-may-2020]
Odada, E.O., 2001. Stable isotopic composition of East African lake waters, International Atomic Energy Agency (IAEA), pp. 43-48.
Otto-Bliesner, B.L., Russell, J.M., Clark, P.U., Liu, Z., Overpeck, J.T., Konecky, B., deMenocal, P., Nicholson, S.E., He, F., Lu, Z., 2014. Coherent changes of southeastern equatorial and northern African rainfall during the last deglaciation. Science 346, 1223-1227.
Rajmohan, N., Elango, L., 2004. Identification and evolution of hydrogeochemical processes in the groundwater environment in an area of the Palar and Cheyyar River Basins, Southern India. Environmental Geology 46, 47-61.
Raymo, M.E., Ruddiman, W.F., Froelich, P.N., 1988. Influence of late Cenozoic mountain building on ocean geochemical cycles. Geology 16, 649-653.
Romaniello, S.J., Field, M.P., Smith, H.B., Gordon, G.W., Kim, M.H., Anbar, A.D., 2015. Fully automated chromatographic purification of Sr and Ca for isotopic analysis. Journal of Analytical Atomic Spectrometry 30, 1906-1912.
Schagerl, M., Renaut, R.W., 2016. Dipping into the Soda Lakes of East Africa, in: Schagerl, M. (Ed.), Soda Lakes of East Africa. Springer, Cham, Switzerland.
Schoell, M., Faber, E., Langguth, H., Pouchan, P., 1976. Survey on the isotopic composition of waters from NE Africa. Geologisches Jahrbuch. Reihe D, Mineralogie, Petrographie, Geochemie, Lagerstaettenkunde, 197-213.
Segele, Z.T., Lamb, P.J., 2005. Characterization and variability of Kiremt rainy season over Ethiopia. Meteorology and Atmospheric Physics 89, 153-180.
Shinjo, R., Chekol, T., Meshesha, D., Itaya, T., Tatsumi, Y., 2011. Geochemistry and geochronology of the mafic lavas from the southeastern Ethiopian rift (the East African Rift System): assessment of models on magma sources, plume–lithosphere interaction and plume evolution. Contributions to Mineralogy and Petrology 162, 209-230.

Skrzypek, G., Mydłowski, A., Dogramaci, S., Hedley, P., Gibson, J.J., Grierson, P.F., 2015. Estimation of evaporative loss based on the stable isotope composition of water using Hydrocalculator. Journal of Hydrology 523, 781-789.
Spooner, E.T.C., 1976. The strontium isotopic composition of seawater, and seawater-oceanic crust interaction, Earth and Planetary Science Letters 31: 1, 167-174.
Stewart, K., Rogers, N., 1996. Mantle plume and lithosphere contributions to basalts from southern Ethiopia. Earth and Planetary Science Letters 139, 195-211.
Street-Perrott, F.A., Harrison, S.P., 1985. Lake level and climate Reconstructions, in: Hecht, A.D. (Ed.), Paleoclimate Analysis and Modeling. John Wiley and Sons, New York, pp. 291-340.
Talbot, M.R., Williams, M.A.J., Adamson, D.A., 2000. Strontium isotope evidence for late Pleistocene reestablishment of an integrated Nile drainage network. Geology 28, 343-346.
Teklay, M., Kröner, A., Mezger, K., Oberhänsli, R., 1998. Geochemistry, Pb□Pb single zircon ages and Nd□Sr isotope composition of Precambrian rocks from southern and eastern Ethiopia: implications for crustal evolution in East Africa. Journal of African Earth Sciences 26, 207-227.
Tekleab, S., Wenninger, J., Uhlenbrook, S., 2014. Characterisation of stable isotopes to identify residence times and runoff components in two meso-scale catchments in the Abay/Upper Blue Nile basin, Ethiopia. Hydrol. Earth Syst. Sci. 18, 2415-2431.
Tenalem, A., Shimeles, F., Wisotzky, F., Demlie, M., Wohnlich, S., 2009. Hierarchical cluster analysis of hydrochemical data as a tool for assessing the evolution and dynamics of groundwater across the Ethiopia rift. International Journal of Physical Sciences 4, 76-90.
Thieblemont, D., 2016. An updated geological map of Africa at 1/10 000 000 scale, 35th International Geological Congress : IGC 2016, Cape Town, South Africa.
Tierney, J.E., deMenocal, P.B., 2013. Abrupt Shifts in Horn of Africa Hydroclimate Since the Last Glacial Maximum. Science 342, 843-846.
Trauth, M.H., Foerster, V., Junginger, A., Asrat, A., Lamb, H.F., Schaebitz, F., 2018. Abrupt or gradual? Change point analysis of the late Pleistocene–Holocene climate record from Chew Bahir, southern Ethiopia. Quaternary Research 90, 321-330.
Trauth, M.H., Maslin, M.A., Deino, A.L., Junginger, A., Lesoloyia, M., Odada, E.O., Olago, D.O., Olaka, L.A., Strecker, M.R., Tiedemann, R., 2010. Human evolution in a variable environment: the amplifier lakes of Eastern Africa. Quaternary Science Reviews 29, 2981-2988.
van der Lubbe, H.J.L., Krause-Nehring, J., Junginger, A., Garcin, Y., Joordens, J.C.A., Davies, G.R., Beck, C., Feibel, C.S., Johnson, T.C., Vonhof, H.B., 2017. Gradual or abrupt? Changes in water source of Lake Turkana (Kenya) during the African Humid Period inferred from Sr isotope ratios. Quaternary Science Reviews 174, 1-12.
Viehberg, F.A., Just, J., Dean, J.R., Wagner, B., Franz, S.O., Klasen, N., Kleinen, T., Ludwig, P., Asrat, A., Lamb, H.F., Leng, M.J., Rethemeyer, J., Milodowski, A.E., Claussen, M., Schäbitz, F., 2018. Environmental change during MIS4 and MIS 3 opened corridors in the Horn of Africa for Homo sapiens expansion. Quaternary Science Reviews 202, 139-153.
Vonhof, H.B., Joordens, J.C.A., Noback, M.L., van der Lubbe, J.H.J.L., Feibel, C.S., Kroon, D., 2013. Environmental and climatic control on seasonal stable isotope variation of freshwater molluscan bivalves in the Turkana Basin (Kenya). Palaeogeography, Palaeoclimatology, Palaeoecology 383-384, 16-26.
West, A.J., Galy, A., Bickle, M., 2005. Tectonic and climatic controls on silicate weathering. Earth and Planetary Science Letters 235, 211-228.
White, A.F., Brantley, S.L., 2003. The effect of time on the weathering of silicate minerals: why do weathering rates differ in the laboratory and field? Chemical Geology 202, 479-506.
Williams, A.P., Funk, C., 2011. A westward extension of the warm pool leads to a westward extension of the Walker circulation, drying eastern Africa. Climate Dynamics 37, 2417-2435.
Woldemariyam, F., Ayenew, T., 2016. Identification of hydrogeochemical processes in groundwater of Dawa River basin, southern Ethiopia. Environ Monit Assess 188:8, 481.
Yitbarek, A., Razack, M., Ayenew, T., Zemedagegnehu, E., Azagegn, T., 2012. Hydrogeological and hydrochemical framework of Upper Awash River basin, Ethiopia: With special emphasis on inter-basins groundwater transfer between Blue Nile and Awash Rivers. Journal of African Earth Sciences 65, 46-60.
Yuretich, R.F., Cerling, T.E., 1983. Hydrogeochemistry of Lake Turkana, Kenya: Mass balance and mineral reactions in an alkaline lake. Geochimica et Cosmochimica Acta 47, 1099-1109.

Acknowledgements

Daniel Gebregiorgis for help in facilitating sample shipment from Ethiopia. Michael Marks at Tübingen University for measuring cation and anions samples. The research is part of the project "Wet Feet or Walking on Sunshine" awarded to AJ, funded by the Ministry of Culture and Science (MWK) of Baden Württemberg, the University of Tübingen and Senckenberg Centre for Human Evolution and Paleoenvironment, Germany.

Author contributions

MM and AJ designed the study. MM, AJ, MLF and BZ conducted fieldwork in Ethiopia, with permissions and access to the sites facilitated by AA and BZ. ANM and MM measured trace elements concentrations, and cations and anions were measured at Tübingen University. DG, SJGG and MM conducted the Sr isotope analyses. MM and HV conducted the stable isotope analyses. GIS and lake-balance modelling were conducted by MM, ANM and MLF. The main manuscript was written by MM and ANM with contributions from all authors.

Figure captions

Figure 1. Panel a: Map of continental Africa where the red box denotes the study region. Panel b: Mean monthly rainfall over the period 1901-2016 CE using the CRU TS 4.01 (land) 0.5° high-resolution grids of monthly climate precipitation observations dataset and compiled in KNMI Climate Explorer (https://climexp.knmi.nl/start.cgi), where the blue circles show the locations of LCB, Lake Abaya (LA) and Lake Chamo (LC), and the yellow star denotes the Ethiopian capital city Addis Ababa. Panel c: Cross section along the East African Rift System from NE to SW, indicating lake level changes in the African Humid

Period relative to today following Junginger and Trauth, 2013. Panel d: Simplified geological map of southern Ethiopian and northern Kenyan catchments. Catchment shapefiles were used to extract the percentage of rock types in the northern Kenyan catchments from the 1:10M-scale geological map of Africa (Thieblemont, 2016) and for southern Ethiopia using the SEAMIC GSE EN Geology 1:2 million scale Geology Map of Ethiopia.

Figure 2. Digital Elevation Model (DEM) of study site indicating the three major lakes investigated: Lake Abaya, Lake Chamo and Lake Chew Bahir. Sampling locations for groundwater (purple squares), lakes (magenta circles), rivers (green diamonds and springs (blue triangles) are indicated on the map. The paleo extent of Lake Chew Bahir is indicated by a black dashed line. Overflow points are shown as yellow stars at the catchment boundaries (Fischer et al., 2020).

Figure 3. Compilation of water stable isotope data from Ethiopia (Ayenew et al., 2008; Bretzler et al., 2011; Cockerton et al., 2013; Darling et al., 1996; Demlie et al., 2007a; Demlie et al., 2007b; Fontes et al., 1970; Furi et al., 2012; Gizaw, 2002; Gonfiantini et al., 1973; IAEA, 2019; Kebede, 2004; Kebede et al., 2005; Kebede et al., 2009; Kebede et al., 2010b; Kebede, 2001; Levin et al., 2009; McKenzie et al., 2001; Mechal et al., 2017; Odada, 2001; Schoell et al., 1976; Tekleab et al., 2014; Yitbarek et al., 2012) and the data collected in this study. Panel a: Scatterplot of $\delta^{2}H$ and $\delta^{18}O$ of rainfall from various sites in Ethiopia including Addis Ababa (n = 362), Addis Ababa West (n = 2), Adu Bariye (n = 5), Alemeya (n = 13), Asela (n = 7), Awassa (n = 19), Butajira (n = 2), Combolcha (n = 7), Dessie (n = 8), Diredawa (n = 12), Hagere Selam (n = 17), Harar (n = 6), Hidolola (n = 4), Kobo (n = 7), Kofele (n = 15), Mega (n = 4), Moyale (n = 4), Neghelle (n =3), Silte (n = 2), Soddo (n = 16), Woldiya (n = 7), Weledi (n = 8), Yavello (n = 3) and Ziway (n = 3) as well as the Global Meteoric Water Line (GMWL) and the calculated Local Meteoric Water Line (LMWL). Calculated mean rainfall value for Lake Chew Bahir was derived from

(https://wateriso.utah.edu/waterisotopes/pages/data_access/form.html). Panel b: Scatterplot of δ^2H and $\delta^{18}O$ of Lakes in the MER, Ethiopia (open circles) and samples from this study (filled circles). Panel c: Scatterplot of δ^2H and $\delta^{18}O$ of groundwater from Ethiopia (open squares) and groundwater wells from the Chew Bahir catchment (filled circles). Panel d: Scatterplot of δ^2H and $\delta^{18}O$ of rivers (open green triangles), hot springs (open red diamonds) and springs (open grey square diamonds) and samples from this study in the Chew Bahir catchment (filled triangles). S1-4 Refers to the position downstream in the Segen River from highest (more upstream) to lowest (less upstream). W1-3 shows the position downstream for the Weyto River. Panel e: Plot of frequency (%) and $\delta^{18}O$ shift from weighted mean rainfall from the Addis Ababa station. Panel f: Plot of frequency (%) and d-excess using the equation d-excess = δ^2H -8* $\delta^{18}O$.

Figure 4. Groundwater and surface water hydrochemistry of the Chew Bahir catchment as well as Lake Abaya (LA) and Lake Chamo (LC) expressed in meq/L (%). Global average rivers (Lowenstein and Risacher, 2009), global average ocean (Lowenstein and Risacher, 2009) and MER Lake hydro-chemistry (Kebede et al., 1994) are also indicated. When Fl or CO_3 data were unavailable it was assumed their input was negligible as Cl and HCO_3 were the dominant anions.

Figure 5. Panel a: Lithological map of the LCB basin and sampling locations. Panel b: Cross plot of $^{87}Sr/^{86}Sr$ and 1/Sr (mmol) showing the end-member mixing zone for LCB (this study) and Lake Turkana (van der Lubbe et al., 2017). Panels c-f: Cross plots of the $^{87}Sr/^{86}Sr$ of LCB catchment surface waters (from Table 2) and the percentage of lithological surface cover. Panels c and d both show moderate but inverse relationships with catchment water $^{87}Sr/^{86}Sr$ and the percentage cover of the catchment in Neogene/Paleogene volcanics and Precambrian basement rocks, respectively. Yellow star in Panel b indicates the mean

composition of all sampled groundwaters, the groundwater end-member used in the lake balance model.

Figure 6. Gibbs plot of hydrological data from this study and regional data for MER lakes (JICA, 2012) and southern Ethiopian groundwaters (Woldemariyam and Ayenew; 2016). Panel a; TDS versus Cl(Cl+HCO_3) and Panel b; TE+DS Na/(Na+Ca), which show the dominance of waters by precipitation, lithology or evaporation process.

Figure 7. Panel a: Cross plot of log Br and log Cl for surface and groundwaters, marine ratio (655±4) (Alcalá and Custodio, 2008) is shown. Panel b: Cross plot of the Na/Cl molar ratio and TDS. Panel c: Cross plot of log Sr and log Cl.

Figure 8. Output from the combined Sr and O model over three different scenarios: Closed terminal LCB, Open terminal LCB and Open flow-through LCB under the conditions described in Table 4. Panel a shows a cartoon of each of the three scenarios. Panel b shows the isotopic (O and Sr) and corresponding LCB lake volume over the three scenarios. The paleo-LCB $^{87}Sr/^{86}Sr$ range of microfossils from van der Lubbe et al. (2017) and Junginger et al. unpublished data are indicated. Further, the points when overflow switches on in the model from Lake Chamo and LCB are indicated. Panel c shows the percentage contributions from each reservoir (LCB: Lake Chew Bahir; GW: groundwater, WR: Weyto River, SR: Segen River, LC: Lake Chamo and P: Precipitation) of dissolved Sr into LCB at the start and end of the modelling period. At the start of the modelling period most of the dissolved Sr is derived from the Weyto (39%) and Segen Rivers (26%), whereas at the end of the modelling period, after a large lake has formed most of the dissolved Sr comes at a single annual time step comes from the LCB itself (the dissolved Sr already present in the lake from the previous time step).

Figure 9. Sr water residence times for LCB for Open terminal LCB and Open flow-through LCB modelling scenarios.

Figure 10. Sensitivity cross-plot of LCB $^{87}Sr/^{86}Sr$ to changes in groundwater/surface water discharge ($R_{Q,\ gw:sw}$) showing the modern, Open terminal LCB and Open flow-through LCB scenarios.

Supplementary

Supplementary Table 1. Model parameters for the initial conditions of the O and Sr model.

Flow Variables	**Q (km^3 a^{-1})**	**Sr (ppb)**	**$^{87}Sr/^{86}Sr$**	**F Sr**	**$\delta^{18}O$**
P	0.0010	-	-	0.00	1.6
E	0.3950	-	-	0.00	-
Weyto River	2.2744	139	0.70611	0.39	-0.87
Segen River	0.7064	299	0.70561	0.26	0.52
Groundwater inflow	0.2502	912	0.70750	0.28	-2.70
Chamo Inflow	0.0000	127	0.70476	0.00	5.36
Lake Chew Bahir	0.1500	394	0.70639	0.07	3.81
Groundwater outflow	2.8371	-	-	-	3.81
Model parameters					
T (∘ C)	30.5	-	-	-	-
h	0.5	-	-	-	-
A	-	-	-	-	-10.11
δ*	-	-	-	-	22.49

Supplementary Table 2. Summary of chemistry data from water samples from the Chew Bahir catchment and Lakes Abaya (LA) and Lake Chamo (LC). Samples in bold denote average values from multiple samples. Sample CB18W2 was a spring sample in a dry river channel. Waterbody's in column 2 refer to rivers (R), springs (S), groundwater (GW) and lakes (L).

Sample ID	Waterbody	Description	N	E	Sampling date	Elevation (m a.s.l.)	Na (mmol/l)	Ca	Mg	K	Cl	F)	Br	PO_4	SO_4	Si	L)	Sr	$^{87}Sr/^{86}Sr$	Sr StErr %	$\delta^{18}O$	$\delta^{2}H$	Alkalinity	pH	EC	TDS	Temp.
							mM	mM	mM	µM	mM	µM	µM	µM	µM	mM	µM	µM	‰	‰	‰	‰	mg/l		µS/cm	mg/l	∘C
CB18W1	R	Segen tributary	37.52627	5.23475	4/11/18	850	1.0	0.9	0.6	74.2	0.2	19.5	0.8	0.6	27.1	0.1	0.5	4.0	0.70547	0.00076	1.2	11.8	178	8.02	420	210	25.6
CB18W2	S (cold)	Segen catchment	37.46492	5.28576	4/11/18	1060	5.2	2.3	0.0	87.0	2.4	35.6	6.4		1939.3	1.0	0.5	14.7	0.70446	0.00040	-1.6	-3.4	484	7.51	1542	771	27.7
CB18W3	R	Segen tributary	37.27096	5.38620	4/11/18	1379	0.8	0.6	0.6	30.7	0.2	16.7	0.4		136.5	0.5	0.6	3.1	0.70450	0.00068	-1.5	-0.5	150	**8.74**	**309.5**	**154.5**	**27.7**
CB18W4	R	Weyto River	37.03264	5.35314	4/11/18	601	0.7	0.4	0.3	28.1	0.1	10.7	0.6	0.8	115.4	0.2	0.6	1.6	0.70615	0.00158	-1.1	2.7	79.4	**8.2**	**206.0**	**102.5**	**28.2**
CB18W5	GW	Hammar Range	36.642097	4.88395	6/11/18	1138	9.7	2.3	4.3	43.5	2.3	156.3	6.3		8130.0	<	7.5	14.1	0.70862	0.00048	-2.7	-8.8	342	**7.0**	**2161.3**	**1080.3**	**29.4**
CB18W6	GW	Hammar Range	36.6469	4.88653	6/11/18	1147	1.5	2.2	2.2	46.0	1.4	51.0	4.3		1587.6	<	6.8	14.6	0.70852	0.00072	-2.7	-9.3	259	**7.1**	**1050.0**	**525.5**	**29.1**
CB18W7	GW	Rift floor	36.852085	4.99075	7/11/18	519	17.7	0.2	0.3	43.5	4.0	128.2	12.1	1.9	3472.8	<	6.7	1.9	0.70635	0.00051	-1.1	2.9	357.5	**7.53**	**2113**	**1056**	**35.2**
CB18W8	R	Weyto tributary	36.87462	5.08736	7/11/18	523	0.8	0.4	0.3	38.4	0.2	15.3	0.7	0.7	150.2	1.5	0.5	2.2	0.70820	0.00113	-0.1	6.8	101.5	7.98	281	140	31.9
CB18W9	L	LCB	36.752075	4.92167	8/11/18	503	2.7	0.9	0.7	140.7	0.7	43.2	2.3	2.5	98.8	<	0.5	4.5	0.70626	0.00047	4.4	26.7	306	7.99	780	390	31.2
CB18W10	GW	Rift floor	36.86254	5.06779	8/11/18	523	21.1	0.9	1.2	89.5	8.9	86.1	20.0	1.3	6927.0	1.6	8.0	6.8	0.70640	0.00044	-1.7	0.2	372	7.44	2805	1402	32.2
CB18W11	R	Weyto River	37.033783	5.26028	9/11/18	567	0.7	0.4	0.3	28.1	0.1	10.9	0.5	1.0	128.2	0.4	0.5	1.6	0.70607	0.00040	-0.9	4.2	95.7	8.29	234	117	33.0
CB18W12	R	Segen River	37.110849	5.20041	9/11/18	581	1.9	0.7	0.5	84.4	0.8	50.0	2.2	1.1	296.8	<	0.6	4.0	0.70549	0.00053	0.5	11.0	171.9	8.46	498	249	30.0
CB18W13	GW	Weyto catchment	36.844368	5.45992	10/11/18	640	2.3	1.2	2.4	104.9	2.4	34.0	6.4		714.9	0.2	5.9	13.7	0.70799	0.00072	-3.4	-13.3		7.21	1090	545	34.7
CB18W14	L	LCB	36.74528	4.98125	15/11/18	504	3.9	0.8	0.7	71.6	0.2	64.9	1.3		16.4	0.0	0.5	4.5	0.70652	0.00131	3.2	24.0	339	7.49	750	375	35.7
CB18W15	GW	Weyto catchment	36.7503515	5.47862	17/11/18	1161	7.6	2.3	3.9	324.8	6.6	79.1	14.4	12.0	951.2	1.7	5.7	11.5	0.71041	0.00071	-1.3	-0.6	707.5	7.33	2069	1035	26.0
CB18W16	R	Segen tributary	37.649975	5.31751	18/11/18	879	0.8	0.5	0.5	51.2	0.2	16.7	0.4		52.4	0.5	0.5	2.7	0.70700	0.00048	0.5	10.3	135	8.02	314	157	29.9
CB18W17	GW	Segen catchment	37.62705	5.322	18/11/18	886	33.1	1.0	1.9	28.1	20.4	91.5	43.3		6352.6	<	5.5	10.2	0.70416	0.00041	-1.2	0.5	663	7.62	4194	2097	31.5

CB18W18	L	LA	37.633595	6.12459	19/11/18	1189	8.4	0.3	0.1	168.8	1.8	405.3	6.0	4.9	193.6	0.1	0.7	1.3	0.70624	0.00046	5.6	41.2	401	9.00	1044	522	28.0
CB18W19	L	LC	37.573742	5.93165	20/11/18	1110	14.3	0.2	0.4	171.4	3.0	355.1	10.0	3.2	188.7	<	4.9	1.6	0.70476	0.00046	5.9	40.6	626	9.13	1611	806	27.3
CB18W20	L	LC	37.54566	5.91948	20/11/18	1110	12.1	0.2	0.4	145.8	2.8	306.7	8.7	3.1	166.7	0.5	0.4	1.3	0.70475	0.00047	4.8	35.0	542	9.11	1269	635	25.9

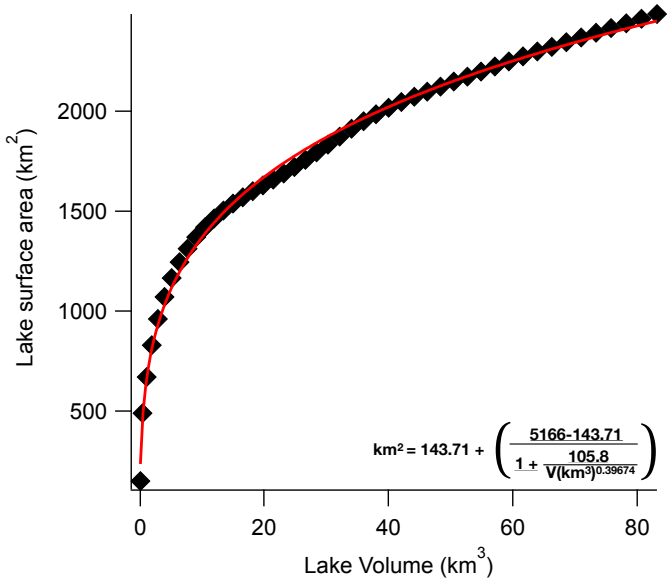

Supplementary Figure 1. Cross plot of volume and surface area for Lake Chew Bahir from the output from Fischer et al. (2020) to solve an equation for lake surface area based on volume (r^2 =0.99).